
μ/π separation using
Convolutional Neural Networks
for the MicroBooNE
Charged Current Inclusive Cross Section
Measurement

Jessica Nicole Esquivel

Bachelor of Science in Electrical Engineering and Applied Physics

St. Mary's University

San Antonio, TX, USA 2011

DISSERTATION

Submitted in partial fulfillment
of the requirements for the degree
Doctor of Philosophy in Physics

- * - DRAFT October 18, 2017 - * -

December, 2017

Syracuse University

Syracuse, New York

Copyright 2017
Jessica Nicole Esquivel
All Rights Reserved
Syracuse University



Abstract

The purpose of this thesis was to use Convolutional Neural Networks (CNN) to separate $\mu's$ and $\pi's$ for use in increasing the acceptance rate of $\mu's$ below the implemented 75cm track length cut in the Charged Current Inclusive (CC-Inclusive) event selection for the CC-Inclusive Cross-Section Measurement. In doing this, we increase acceptance rate for CC-Inclusive events below a specific momentum range.

Dedication

I dedicate this dissertation to the two important women in my life; My wife and my mom. Both have been there cheering me on giving me strength and love as I worked towards the hardest accomplishment I've ever done.

Jessica Nicole Esquivel

Acknowledgements

Of the many people who deserve thanks, some are particularly prominent, such as my supervisor...

Contents

List of figures	xiii
List of tables	xix
1. Introduction	1
2. Neutrinos	3
2.1. What are Neutrinos	3
2.2. History of Neutrinos	4
2.3. Neutrino Oscillations	4
2.3.1. Solar Oscillations and the Solar Neutrino Problem	5
2.3.2. Atmospheric Oscillations and the Atmospheric Neutrino Anomaly	7
2.3.3. Two Flavor Neutrino Oscillation Formulation	9
2.3.4. Three Flavor Neutrino Oscillation Formulation	12
2.3.5. Reactor Oscillation	13
3. The MicroBooNE Experiment	15
3.1. Liquid argon time projection chambers	15
3.2. The MicroBooNE Time Projection Chamber	16
3.3. MicroBooNE's Physics Goals	18
3.3.1. The low-energy excess	18
3.3.2. Cross sections	19
3.3.3. Astroparticle physics	19
3.3.4. Liquid argon detector development	19
4. The Booster Neutrino Beam	21
4.1. Creating the Booster Neutrino Beam	21
5. Neutrino Identification: Finding MicroBooNE's first Neutrinos	23

6. CC-Inclusive Cross Section Selection Filter	25
7. The importance of μ/π separation in MicroBooNE	29
8. Convolutional Neural Networks	31
9. Hardware Frameworks	35
9.1. Syracuse CPU Machine setup	35
9.2. Syracuse University GPU Cluster Setup	35
10. Using Convolutional Neural Networks to separate μ's from π's	37
10.1. Image Making Scheme	37
10.2. Convolutional Neural Network Training	39
10.3. Classification of MC data using Selection I Original CC-Inclusive Filter	40
10.4. Classification of MC data using Selection I Modified CC-Inclusive Filter	45
10.5. Conclusions and Future Work	53
11. Using Convolutional Neural Networks on MicroBooNE Data	57
12. Comparing two CC-Inclusive Cross Section Selection Filters	59
13. Conclusion	61
A. Pointless extras	63
A.1. Like, duh	63
A.2. $y = \alpha x^2$	63
Bibliography	65

List of figures

2.1. The Standard Solar Model	5
2.2. Solar Neutrino Experiments	7
2.2a. Ray Davis's Homestake Experiment	7
2.2b. Kamiokande Experiment	7
2.2c. SNO Experiment	7
2.3. Cosmic Ray Shower	8
2.4. Measurements of the double ratio for various atmospheric neutrino experiments	9
2.5. The flavor eigenstates are rotated by an angle θ with respect to the mass eigenstates	10
4.1. 4.1b Flux of BNB at FNAL.	22
4.1a. Low Energy excess seen in MiniBooNE	22
4.1b. Energy spectrum of the Booster Neutrino Beam at Fermi Na- tional Laboratories	22

6.1.	6.1a Track range distribution for selection I. The track range is defined as the 3D distance between the start and end of the muon candidate track. No data is shown below 75 cm due to the track length cut described previously. 6.1b Efficiency of the selected events by process quasi-elastic (QE), resonant (RES), and deep-inelastic (DIS). Statistical uncertainty is shown in the bands and the distributions are a function of true muon momentum. The rise of the efficiency between 0 GeV and 0.5 GeV is due to the minimum track length cut and the decreasing efficiency for higher momentum tracks is caused by the containment requirement. .	27
6.1a.	Track range distribution of selection I	27
6.1b.	Selection efficiency as a function of the true muon momentum .	27
8.1.	Applying a feature mask over a set of fashion items to extract necessary information for auto-encoding. Unnecessary information for example color or brand emblems are not saved. This feature map is an edge detection mask that leaves only shape information which helps to distinguish between different types of clothes.	32
8.2.	Pictorial Representation of Convolutional Neural Networks as well as a visual representation on CNN's complexity of layer feature extraction	33
10.1.	Accuracy vs. Loss of ImageNet 2-output μ/π sample consisting of 10000 images each.	40
10.2.	Description of confusion matrix variables: False pion rate = $false\pi/total\pi$ True pion rate = $true\pi/total\pi$ Accuracy = $(true\pi rate + true\mu rate)/2$ Pion prediction value = $true\pi/(true\pi + false\pi)$ Muon prediction value = $true\mu/(true\mu + false\mu)$ 10.2c The probability plot includes muons and pions that are classified as primary particles.	41
10.2a.	Confusion Matrix showing Accuracy of CNN using training data	41
10.2b.	Confusion Matrix showing Accuracy of CNN using testing data	41
10.2c.	Probability plot of muons and pions from testing set. Images surrounding histogram are a random event from lowest bin and highest bin for each particle.	41

10.3. Snapshot of passing rates of Selection I from CC-Inclusive Filter	42
10.4. Results of CNN10000 classification of track candidate images output from cc-inclusive filter.	43
10.4a. Confusion Matrix showing Accuracy of CNN using data with wrong normilazion	43
10.4b. Probability plot showing μ/π separation of CNN using wrong normalization	43
10.4c. Confusion Matrix showing Accuracy of CNN using data with correct normilazion	43
10.4d. Probability plot showing μ/π separation of CNN using correct normalization	43
10.5. CNN10000 distributions of track candidate images output from Selection I Original cc-inclusive filter with different image data normalizations	44
10.5a. Track range distribution of events from Selection I Original passing CNN with 70% accuracy using image data with wrong normilazion	44
10.5b. Track range distribution of events from Selection I Original passing CNN with 70% accuracy using image data with correct normilazion	44
10.5c. Momentum distribution of events from Selection I Original passing CNN with 70% accuracy using image data with wrong normilazion	44
10.5d. Momentum distribution of events from Selection I Original passing CNN with 70% accuracy using image data with correct normilazion	44
10.6. Snapshot of passing rates of all cuts from Selection I Modified cc-inclusive filter	45
10.7. Confusion matrix and probability plot of events passing selection I modified cc-inclusive cuts right before 75cm track length cut	47

10.7a. Confusion Matrix for CNN10000 classified events from selection I modified	47
10.7b. Probability plot for CNN10000 classified events from selection I modified	47
10.8. CNN10000 distributions of track candidate images output from Selection I Modified cc-inclusive filter	48
10.8a. Track range distribution of events from Selection I Modified passing CNN with 70% accuracy	48
10.8b. Stacked signal and background track range distributions from Selection I Modified passing CNN with 70% accuracy	48
10.8c. Stacked signal and background track range distributions from Selection I Modified passing 75 cm track length cut	48
10.8d. Stacked signal muons and background muons/pions of track range distributions from Selection I Modified passing CNN with 70% accuracy	48
10.8e. Stacked signal muons and background muons/pions of track range distributions from Selection I Modified passing 75 cm track length cut	48
10.9. CNN10000 stacked signal/background track range distributions of track candidate images output from Selection I Modified cc-inclusive filter	49
10.9a. Stacked signal muons and background muons/pions of track range distributions from Selection I Modified passing CNN with 75% accuracy	49
10.9b. Stacked signal muons and background muons/pions of track range distributions from Selection I Modified passing CNN with 80% accuracy	49
10.9c. Stacked signal muons and background muons/pions of track range distributions from Selection I Modified passing CNN with 85% accuracy	49

10.9d. Stacked signal muons and background muons/pions of track range distributions from Selection I Modified passing CNN with 90% accuracy	49
10.10CNN10000 momentum distributions of track candidate images output from Selection I Modified cc-inclusive filter	50
10.10a. Momentum distribution of events from Selection I Modified passing CNN with 70% accuracy	50
10.10b. Stacked signal and background momentum distributions from Selection I Modified passing CNN with 70% accuracy	50
10.10c. Stacked signal and background momentum distributions from Selection I Modified passing 75 cm track length cut	50
10.11Track distribution comparisons of true CC muons plotted vs true CC muons and pions plotted	51
10.11a. Stacked signal μ /background μ and π track range distribution of CNN @ 70%	51
10.11b. Stacked signal μ & π /background μ & π track range distribution of CNN @ 70%	51
10.12Images of true CC events where the pion was the tagged track candidate	51
10.12a. Pion reconstructed track range is less than 75 cm and longer than muon track due to dead wires	51
10.12b. Pion reconstructed track range is less than 75 cm and larger than muon reconstructed track	51
10.12c. Pion reconstructed track range is greater than 75 cm and larger than muon reconstructed track	51
10.13Snapshot of signal and background event numbers of Selection I modified from cc-inclusive note [?]	54
10.14CNN performance of classified muons and pions compared to the already implemented 75 cm track length cut	54

List of tables

10.1. Comparing passing rates of CNN at different probabilities versus 75 cm track length cut: Numbers are absolute event counts and Cosmic background is not scaled appropriately. The BNB+Cosmic sample contains all events. The numbers in brackets give the passing rate wrt the step before (first percentage) and wrt the generated events (second percentage). In the BNB+Cosmic MC Truth column shows how many true ν_μ CC-inclusive events (in FV) are left in the sample. This number includes possible mis-identifications where a cosmic track is picked by the selection instead of the neutrino interaction in the same event. The CNN MC True generated events were scaled wrt the MC True generated events for the 75 cm cut passing rates due to only running over 188,880 generated events versus the 191362 generated events. The last column Signal:Cosmic only gives an estimate of the ν_μ CC events wrt the cosmic only background at each step. For this number, the cosmic background has been scaled as described in [?]. Note that these numbers are not a purity, since other backgrounds can't be determined at this step. . .	52
10.2. Signal and background event numbers at modified selection level with CNN cut estimated from a BNB+Cosmic sample and Cosmic only sample normalized to $5 * 10^{19}$ PoT. The last column gives the fraction of this signal or background type to the total selected events per CNN probability.	52

*“If the don’t give you a seat at the table,
bring a folding chair.”*

— Shirley Chisholm

Chapter 1.

Introduction

This thesis will be a description of work done to further increase efficiency and purity of the charged current inclusive cross section measurement using the MicroBooNE detector. It will also describe the MicroBooNE detector, what neutrinos are, the charged current inclusive cross section measurement and its importance as well as convolutional neural networks and how they can be used in μ/π separation. Chapter 2 will talk about the background of neutrinos and the people and detectors that discovered neutrinos as well as an in depth history of neutrino oscillation and the discovery that neutrinos have mass. Chapter 3 will discuss the MicroBooNE experiment, specifically, how Liquid Argon Time Projection Chambers work, the Light Collection System and the Electronic and Readout Trigger systems. Chapter 4 will describe the Booster Neutrino Beam stationed at Fermi National Accelerator Lab. It will go into depth on the neutrino flux and ... Chapter 5 will discuss the work I did on detecting the first neutrinos seen in the MicroBooNE detector and the software reconstruction efforts required to create an automated neutrino ID filter that was used to find the first neutrinos and then was later expanded on to create the charged current inclusive filter that will be discussed in chapter 6 Chapter 7 will discuss the importance of μ/π separation for the charged current inclusive cross section measurement. Chapter 8 will give a brief description of what Convolutional Neural Networks are and how it will be used for μ/π separation in this selection. Chapter 9 will discuss hardware Chapters 10, 11 and 12 will discuss the results of using Convolutional Neural Networks on monte-carlo and data to sift out charged current inclusive neutrino events.

Chapter 2.

Neutrinos

2.1. What are Neutrinos

Neutrinos are one of the fundamental particles which make up the universe. They are also one of the least understood. Neutrinos are not affected by the electromagnetic forces because they do not have electric charge. Neutrinos are affected by a "weak" sub-atomic force of much shorter range than electromagnetism, and are therefore able to pass through great distances in matter without being affected by it. Until the late 90's, neutrinos were thought to have no mass. Due to their mass, neutrinos are also affected by gravity. Neutrinos are created by radioactive decay or nuclear reactions such as the ones that happen in the sun, in nuclear reactors or when cosmic rays hit atoms. There are three types of neutrinos, ν_e , ν_μ and ν_τ which correspond to their charged lepton pairs.

As previously stated, neutrinos are very weakly interacting; in fact, neutrinos can pass unscathed through a wall of lead several hundred light-years thick. Because neutrinos interact so rarely, studying neutrinos requires a massive detector and a powerful neutrino source. With that being said, we can only infer their existence when they interact in a detector. In a collision, distinct charged particles are produced with each type of neutrino. An electron neutrino will create an electron, a muon neutrino will create a muon, and a tau neutrino will create a tau. The track the particle leaves in the detector is how one figures out what type of neutrino interaction was "seen". Liquid Argon Time Projection Chambers are the newest type of detectors being used to study neutrinos due to their excellent imaging and particle identification capabilities.

2.2. History of Neutrinos

The neutrino was first postulated by Wolfgang Pauli in 1931 to explain how beta decay could resolve the conservation of energy, momentum and angular momentum problem. Pauli suggested that this missing energy might be carried off, unseen, by a neutral particle (he called neutron) which was escaping detection. James Chadwick discovered a much heavier nuclear particle in 1932 that he also named neutron, leaving two particles with the same name. Enrico Fermi was the first person to coin the term neutrino (which means little neutral one in latin) in 1933 to fix this confusion. Fermi's paper, which was published in 1934, unified Pauli's neutrino with Paul Dirac's positron and Werner Heisenberg's neutron-proton model and his theory accurately explained many experimentally observed results. Wang Ganchang first proposed the use of beta capture to experimentally detect neutrinos and in 1959 Clyde Cowan and Frederick Reines published their work stating that they had detected the neutrino. The experiment called for antineutrinos created in a nuclear reactor by beta decay that reacted with protons producing neutrons and positrons: $\nu_e + p^+ \rightarrow n^0 + e^+$. Once this happens, the positron finds an electron and they annihilate each other and the resulting gamma rays are detectable. The neutron is detected by neutron capture and the releasing of another gamma ray. In 1962 Leon M. Lenderman, Melvin Schwartz and Jack Steinberger were the first to detect interactions of the muon neutrino. The first detection of the tau neutrino was announced in the summer of 2000 by the DONUT collaboration at Fermilab. In the late 1960s, many experiments found that the number of electron neutrinos arriving from the sun was around 1/3 to 1/2 the number predicted by the Standard Solar Model. This became known as the solar neutrino problem and remained unresolved for around thirty years. This problem was resolved by the discovery of neutrino oscillation and mass. [1]

2.3. Neutrino Oscillations

Neutrino oscillation was first predicted by Bruno Pontecorvo. It describes the phenomenon of a neutrino created with a specific lepton flavor (electron, muon or tau) that is later measured to have a different flavor. Neutrino oscillation is important theoretically and experimentally due to the fact that this observation implies that the neutrino has a non-zero mass, which is not part of the original Standard Model of particle physics. [2]

2.3.1. Solar Oscillations and the Solar Neutrino Problem

The solar neutrino flux derived from Bahcall's Standard Solar Model is shown in figure 2.1. Nuclear fusion and decay processes produce an abundant amount of neutrinos. The standard solar model predicts that these reactions produce several groups of neutrinos, each with differing fluxes and energy spectra. The figure also shows the ranges of detection of existing solar neutrino experiments in different shades of blue to illustrate that they sample different portions of the solar neutrino energy spectrum. Three of these experiments, plus a new one, are discussed below.

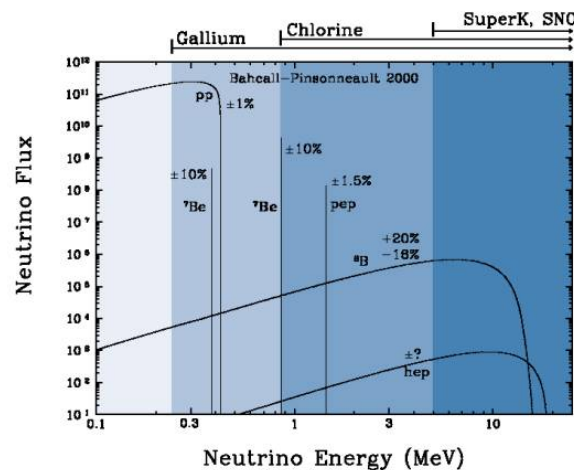


Figure 2.1.: The Standard Solar Model

Since neutrinos rarely interact with matter, they pass through the sun and the earth undetected. About 65-billion neutrinos from the sun stream through every square centimeter on the Earth every second, yet we are oblivious to their passage in our every-day lives. [3]

The first experiment to detect the effects of neutrino oscillation was the Ray Davis's Homestake Experiment. The detector was stationed in the Homestake Gold Mine in Lead, South Dakota. It was 1,478 meters underground and was 380 m^3 . The detector was filled with perchloroethylene. Perchloroethylene was chosen because of its high concentrations of chlorine. When an ν_e interacted with chlorine-37 atom, the atom would transform to argon-37 which was then extracted and counted. The neutrino capture reaction is shown in equation 2.1. Davis observed a deficit of about 1/3 the flux of solar neutrinos that was predicted by Bahcall's Standard Solar Model.

The unexplained difference between the measured solar neutrino flux and model predictions lead to the Solar Neutrino Problem. [4]



While it is now known that the Homestake Experiment detected neutrinos, some physicist were weary of the results. Conclusive evidence of the Solar Neutrino Problem was provided by the Kamiokande-II experiment, a water Cherenkov detector with a low enough energy threshold to detect neutrinos through neutrino-electron elastic scattering. In the elastic scattering interaction the electrons coming out of the point of reaction strongly point in the direction that the neutrino was traveling, away from the sun. While the neutrinos observed in Kamiokande-II were clearly from the sun, there was still a discrepancy between Kamiokande-II and Homestake; The Kamiokande-II experiment measured about 1/2 the predicted flux, rather than the 1/3 that the Homestake Experiment saw.

The solution to the solar neutrino problem was finally experimentally determined by the Sudbury Neutrino Observatory(SNO). The Ray Davis's Homestake Experiment was only sensitive to electron neutrinos, and the Kamiokande-II Experiment was dominated by the electron neutrino signal. The SNO experiment had the capability to see all three neutrino flavors. Because of this, it was possible to measure the electron neutrinos and total neutrino flux. The experiment demonstrated that the deficit was due to the MSW effect, the conversion of electron neutrinos from their pure flavor state into the second neutrino mass eigenstate as they passed through a resonance due to the changing density of the sun. The resonance is energy dependent, and is visible near 2MeV. The water cherenkov detectors only detect neutrinos above about 5MeV, while the radiochemical experiments were sensitive to lower energy (0.8MeV for chlorine, 0.2MeV for gallium), and this turned out to be the source of the difference in the observed neutrino rates at the two types of experiments. Figure 2.2 shows Homestake, Kamiokande-II and SNO experiments.

MSW Effect

The Mikheyev-Smirnov-Wolfenstein effect is a process which acts to modify neutrino oscillations in matter. The presence of electrons in matter changes the energy

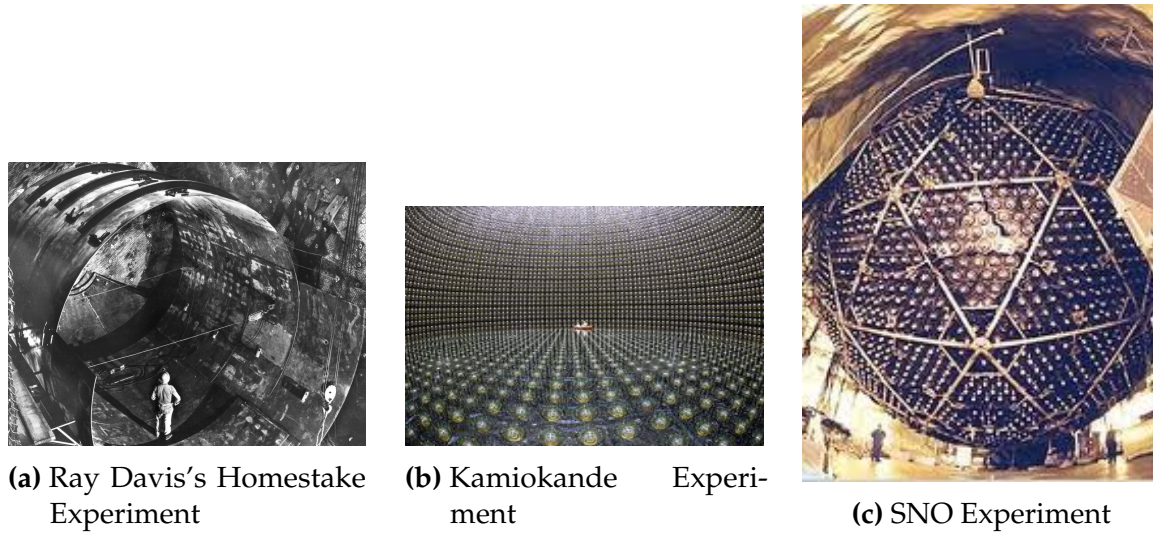


Figure 2.2.: Solar Neutrino Experiments

levels of the mass eigenstates of neutrinos due to charged current coherent forward scattering of the electron neutrinos. This coherent forward scattering is similar to the electromagnetic process with respect to the refractive index of light in a medium. Because of this MSW Effect, neutrinos in vacuum have a different effective mass than neutrinos in matter and because neutrino oscillations depend on the squared mass difference of the neutrinos, the neutrino oscillations are different in matter than in vacuum. This effect is important at the sun where electron neutrinos are produced. The neutrinos of high energy leaving the sun are in a vacuum propagation eigenstate ν_2 that has a very small overlap with the electron neutrino $\nu_e = \nu_1 \cos(\theta) + \nu_2 \sin(\theta)$ seen by the charged current reactions in Kamiokande-II and SNO. The discrepancy of the deficit between SNO, Kamiokande-II and Homestake is due to the energy of the solar neutrinos. The MSW effect "turns on" at about 2MeV and at lower energies, this MSW effect is negligible. [5]

2.3.2. Atmospheric Oscillations and the Atmospheric Neutrino Anomaly

Atmospheric neutrinos are neutrinos that stem from the decay hadrons coming from primary cosmic rays. The dominant part of the decay chain is shown in equations 2.2 and 2.3

$$\pi^+ \rightarrow \mu^+ \nu_\mu \mu^+ \rightarrow e^+ \nu_e \bar{\nu}_\mu \quad (2.2)$$

$$\pi^- \rightarrow \mu^- \bar{\nu}_\mu \mu^- \rightarrow e^- \bar{\nu}_e \nu_\mu \quad (2.3)$$

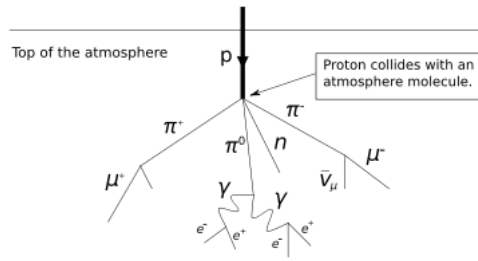


Figure 2.3.: Cosmic Ray Shower

Figure 2.3 shows the cosmic ray shower. In general, these neutrinos have energies from 1GeV to 100s of GeV and the ratio of ν_μ s to ν_e s equals to 2 (see equation 2.4)

$$R = \frac{(\nu_\mu + \bar{\nu}_\mu)}{(\nu_e + \bar{\nu}_e)} \quad (2.4)$$

There have been two types of detectors used to study atmospheric neutrinos: Water Cherenkov detectors and tracking calorimeters. Super-Kamiokande is the detector we will focus on. These atmospheric detector experiments measure the ratio of ν_μ to ν_e . They also measure the zenith angle distribution of the neutrinos. These experiments report a double ratio (shown in equation 2.5). This double ratio is the ratio measured in the detector to the ratio that's expected which is 2. If the double ratio equals to 1, the data agrees with the prediction. Various measurements from multiple experiments are shown in figure 2.4. Except for Frejus, all R measurements are less than 1. This discrepancy between the predicted R and the measured R became known as the Atmospheric Neutrino Anomaly.

$$R = \frac{(N_\mu/N_e)_{DATA}}{(N_\mu/N_e)_{SIM}} \quad (2.5)$$

Kamiokande-II has the capability of measuring the direction of the incoming neutrinos. The expectation of atmospheric neutrino detection is that the flux be

Experiment	Type of experiment	R
Super-Kamiokande	Water Cerenkov	0.675 ± 0.085
Soudan2	Iron Tracking Calorimeter	0.69 ± 0.13
IMB	Water Cerenkov	0.54 ± 0.12
Kamiokande	Water Cerenkov	0.60 ± 0.07
Frejus	Iron Tracking Calorimeter	1.0 ± 0.15

Figure 2.4.: Measurements of the double ratio for various atmospheric neutrino experiments

isotropic due to the fact that atmospheric neutrinos can reach the detector from all directions. Kamiokande-II noticed that muon-like data did not agree well with this expectation. At low energies approximately half of the ν_μ are missing over the full range of zenith angles. At high energies the number of ν_μ coming down from above the detector seems to agree with expectation, but half of the same ν_μ coming up from below the detector are missing. This anomaly can be easily explained by neutrino flavor oscillations. Due to the fact that the neutrino travels less distance coming straight down into the detector (about 15km) than coming up from the bottom of the detector(13000km) changes the probability of oscillation. The probability of oscillation for the muon neutrinos coming down into the detector is roughly zero, whereas for neutrinos coming up, the oscillation probability is $\sin^2(2\theta)$. Both the solar and atmospheric neutrino problems can be explained by neutrino oscillation so its fitting to derive this phenomenon mathematically. In the next two sections, two flavor and three flavor neutrino oscillation derivations will be explained.

2.3.3. Two Flavor Neutrino Oscillation Formulation

The flavor eigenstates can oscillate between eachother because they are composed of an add-mixture of mass eigenstates(ν_1, ν_2). Figure 2.5 shows the mass and flavor eigenstates rotated by an angle θ which is the mixing angle.

In matrix form the wavefunctions are:

$$\begin{pmatrix} \nu_\mu \\ \nu_e \end{pmatrix} = \begin{pmatrix} \cos\theta & \sin\theta \\ -\sin\theta & \cos\theta \end{pmatrix} * \begin{pmatrix} \nu_1 \\ \nu_2 \end{pmatrix} \quad (2.6)$$

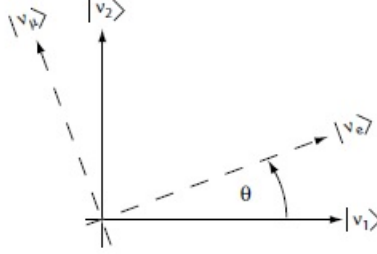


Figure 2.5.: The flavor eigenstates are rotated by an angle θ with respect to the mass eigenstates

Applying the time evolution operator to ν_μ :

$$|\nu_\mu(t)\rangle = -\sin\theta|\nu_1\rangle e^{-i\frac{E_1 t}{\hbar}} + \cos\theta|\nu_2\rangle e^{-i\frac{E_2 t}{\hbar}} \quad (2.7)$$

where $E_1 = \sqrt{p^2 c^2 + m_1^2 c^4}$ and $E_2 = \sqrt{p^2 c^2 + m_2^2 c^4}$ and $p_1 = p_2$. For the time being, let us assume $\hbar = c = 1$. With this assumption: $E_1 = \sqrt{p^2 + m_1^2}$ and $E_2 = \sqrt{p^2 + m_2^2}$. The next modification is to assume neutrinos are relativistic:

$$\gamma = \frac{E}{m_o c^2} = \frac{\sqrt{p^2 c^2 + m_o^2 c^4}}{m_o c^2} \gg 1 \quad (2.8)$$

because of this,

$$p \gg m_o \quad (2.9)$$

$$E = \sqrt{p^2 + m_o^2} = p\sqrt{1 + m_o^2/p^2} \simeq p + \frac{1}{2} \frac{m_o^2}{p} \quad (2.10)$$

where the binomial expansion is used. Now E_1 and E_2 can be written as:

$$E_1 \simeq p + \frac{1}{2} \frac{m_1^2}{p} \text{ and } E_2 \simeq p + \frac{1}{2} \frac{m_2^2}{p} \quad (2.11)$$

Now applying all these assumptions back into equation 2.7 gives us:

$$|\nu_\mu(t)\rangle = -\sin\theta|\nu_1\rangle e^{-i\left(p + \frac{1}{2} \frac{m_1^2}{p}\right)t} + \cos\theta|\nu_2\rangle e^{-i\left(p + \frac{1}{2} \frac{m_2^2}{p}\right)t} \quad (2.12)$$

$$|\nu_\mu(t)\rangle = e^{-i\left(p + \frac{1}{2}\frac{m_1^2 - m_2^2}{p}\right)t} (-\sin\theta|\nu_1\rangle + \cos\theta|\nu_2\rangle) \quad (2.13)$$

Substituting $\Delta m^2 = m_1^2 - m_2^2$ and $t = \frac{x}{c} = x$ and $e^{-iz} = e^{-i\left(p + \frac{1}{2}\frac{m_1^2}{p}\right)t}$ gives us:

$$|\nu_\mu(t)\rangle = e^{-iz} \left(-\sin\theta|\nu_1\rangle + \cos\theta|\nu_2\rangle e^{+ix\left(\frac{1}{2}\frac{\Delta m^2}{p}\right)} \right) \quad (2.14)$$

Finding the Probability for a $\nu_\mu \rightarrow \nu_e$:

$$P(\nu_\mu \rightarrow \nu_e) = |\langle \nu_e | \nu_\mu(t) \rangle|^2 \quad (2.15)$$

Remembering that $\langle \nu_i | \nu_j \rangle = \delta_{ij}$

$$\langle \nu_e | \nu_\mu(t) \rangle = e^{-iz} \left(-\sin\theta\cos\theta + \sin\theta\cos\theta e^{\frac{i\Delta m^2 x}{p}} \right) \quad (2.16)$$

Taking the absolute value squared gives us:

$$P(\nu_\mu \rightarrow \nu_e) = |\langle \nu_e | \nu_\mu(t) \rangle|^2 = e^{+iz} e^{-iz} \sin^2\theta \cos^2\theta \left(-1 + e^{\frac{i\Delta m^2 x}{p}} \right) \left(-1 + e^{\frac{i\Delta m^2 x}{p}} \right) \quad (2.17)$$

Since the neutrino is relativistic we can set $p = E_\nu$ and change $x = L$. Also recognizing the trigonometric relation $(1 - \cos 2\theta)/2 = \sin^2\theta$ the above equation becomes:

$$P(\nu_\mu \rightarrow \nu_e) = \sin^2 2\theta \sin^2 \left(\frac{\Delta m^2 L}{4E_\nu} \right) \quad (2.18)$$

All that's left to do now is re-introduce \hbar and c doing this we get:

$$P_{\nu_\mu \rightarrow \nu_e}(L, E) = \sin^2 2\theta \sin^2 \left(1.27 \Delta m^2 \frac{L}{E_\nu} \right) \quad (2.19)$$

This equations has three important variables.

- The angle θ : This angle, as mentioned before, is called the mixing angle. It defines the difference between the flavor and the mass eigenstates. When $\theta = 0$ the mass and flavor eigenstates are identical and now oscillations occur.
- The mass squared difference, Δm^2 : Again $\Delta m^2 = m_1^2 - m_2^2$. The reason this is an important variable is because it implies that for neutrinos to oscillate, neutrinos must have mass. Furthermore, the mass squared difference also tells us that the neutrino mass eigenstates must be different.
- L/E: This is the variable that is of most interest to experimental physicists due to the fact that it is the variable that we set. L is the distance between the source and detector and E is the energy of the neutrino. For a given Δm^2 , the probability of oscillation changes with respect to L/E.

2.3.4. Three Flavor Neutrino Oscillation Formulation

Seeing the quantum mechanics involved in deriving the probability of a two flavor neutrino oscillation, it is now possible to formulate the three flavor neutrino oscillation. The three flavor neutrino oscillation formulation begins similarly to the two flavor, but there is the Pontecorvo-Maki-Nakagawa-Sakata matrix (PMNS) instead of the 2X2 matrix in the previous section. The PMNS matrix is show below:

$$\begin{pmatrix} c_{12}c_{13} & s_{12}c_{13} & s_{13}e^{-i\delta} \\ -s_{12}c_{23} - c_{12}s_{23}s_{13}e^{i\delta} & c_{12}c_{23} - s_{12}s_{23}s_{13}e^{i\delta} & s_{23}c_{13} \\ s_{12}s_{23} - c_{12}c_{23}s_{13}e^{i\delta} & -c_{12}s_{23} - s_{12}c_{23}s_{13}e^{i\delta} & c_{23}c_{13} \end{pmatrix} * \begin{pmatrix} e^{i\alpha_1/2} & 0 & 0 \\ 0 & e^{i\alpha_2/2} & 0 \\ 0 & 0 & 1 \end{pmatrix} \quad (2.20)$$

where $c_{ij} = \cos\theta_{ij}$ and $s_{ij} = \sin\theta_{ij}$

Following the same steps as before we get:

$$P_{\alpha \rightarrow \beta} = \delta_{\alpha\beta} - 4\sum \text{Re}(U_{\alpha i}^* U_{\beta i} U_{\alpha j} U_{\beta j}^*) \sin^2 \left(\frac{\Delta m_{ij}^2 L}{4E} \right) + 2\sum \text{Im}(U_{\alpha i}^* U_{\beta i} U_{\alpha j} U_{\beta j}^*) \sin \left(\frac{\Delta m_{ij}^2 L}{2E} \right) \quad (2.21)$$

The main things to notice here are δ_{ij} which is the CP violating term and has not been measured yet, and θ_{13} which has just been measured. CP violation is a violation

of the postulated CP-symmetry. CP-symmetry states that the laws of physics should be the same if a particle were to be exchanged with its antiparticle and then if the left hand side of a decay were switched with the right hand side.

2.3.5. Reactor Oscillation

Many experiments have searched for oscillation of electron anti-neutrinos produced at nuclear reactors. Such oscillations give the value of the parameter θ_{13} . The KamLAND experiment, started in 2002, has made a high precision observation of reactor neutrino oscillation. Neutrinos produced in nuclear reactors have energies similar to solar neutrinos, a few MeV. The baselines of these experiments have ranged from tens of meters to over 100 km. On 8 March 2012, the Daya Bay team announced a 5.2σ discovery that $\theta_{13} \neq 0$.

Chapter 3.

The MicroBooNE Experiment

The purpose of this chapter is to discuss and understand the details of the MicroBooNE detector. A thorough understanding of MicroBooNE and the technology behind liquid argon time projection chambers is important for understanding results as well as understanding how images were made for use in deep learning efforts that will be outlined in later chapters.

3.1. Liquid argon time projection chambers

Liquid Argon Time Projection Chambers (LArTPCs) are an exciting detector technology that provide excellent imaging and particle identification, and are now being used to study neutrinos. The Time Projection Chamber (TPC) was first invented by Nygren in 1974 [?] and the proposal for a LArTPC for neutrino physics was made by Rubbia [?] in 1977 with the ICARUS collaboration implementing this concept [?]. A LArTPC is a three-dimensional imaging detector that uses planes of wires at the edge of an active volume to read out an interaction. When a neutrino interacts with an argon atom, the charged particles that are produced ionize the LAr as they travel away from the interaction. By placing a uniform electric field throughout the LAr volume, the ionization is made to drift towards a set of anode planes, which consist of wires spaced very closely together collecting the ionized charge, which is subsequently read out by electronics connected to the anode wires. The collected ionization creates a spatial image of what happened in the detector on each anode plane. The position resolution of the interaction along the beam direction (perpendicular to drift direction) relies on the wire pitch, while the resolution in drift direction is dependent on the

timing resolution of the electronics used and the longitudinal diffusion in the volume. The drift time of the ionization relative to the time of the original signal allows the signal to be projected back along the drift coordinate, hence the name LArTPC. Having very small distances between each wire within an anode plane allows for very fine granularity and detail to be captured, and having multiple wire planes at different angles provides independent two-dimensional views that can be combined into a three dimensional picture of the interaction. Once the charge signal is created on the anode planes, software analysis packages identify particles in the detector by using deposited energy on the wires along their track length. The 30 year development of the ICARUS detector has led to LArTPCs being used as cosmic ray [?], solar neutrino [?] and accelerator neutrino [?] detectors. The ArgoNeuT experiment at Fermilab was the first United States based liquid argon neutrino program that has since produced short-baseline $\nu - Ar$ cross-section measurements in the NUMI beamline [?]. The MicroBooNE experiment is the second experiment in the US based LArTPC neutrino program and will be discussed thoroughly in the next sections. The next phases of the liquid argon neutrino program are under way and are the Fermilab Short Baseline Neutrino (SBN) program [?] and the Deep Underground Neutrino Experiment (DUNE) [6]. The SBN program will include three LArTPC detectors, including the MicroBooNE detector, on the Booster Neutrino Beam (BNB) to do multiple-baseline oscillation measurements. The detector closest to the beam will be the 40 ton Short Baseline Neutrino Detector (SBND) [?] at 150 m and the detector furthest is the 600 ton ICARUS T600 [?] detector positioned at 600 m. The DUNE collaboration will deliver a 30 GeV neutrino beam 1300 km from Fermilab to a 34 kiloton LArTPC detector at Homestake, SD. DUNE will study the leptonic CP phase, δ_{cp} , as well as measure neutrino and antineutrino oscillations.

3.2. The MicroBooNE Time Projection Chamber

MicroBooNE (Micro Booster Neutrino Experiment) is a 89 ton active volume (180 ton total mass) LArTPC which is then inserted into a cylindrical cryostat on axis of the Booster Neutrino Beam (BNB) stationed at Fermilab in Batavia, Illinois. Understanding LArTPC technology and detector physics is necessary to build a LArTPC the size of DUNE, and MicroBooNE has made many advances in developing this technology [7] [8].

MicroBooNE's Time Projection Chamber (TPC) is 10.3 m long (beamline direction), 2.3 m high and 2.5 m wide (which corresponds to the drift distance). The TPC is shown in figure ???. MicroBooNE is the largest LArTPC currently running in the world [9]. This LArTPC has 3 wire planes: 1 plane that collects the ionization in the wires and is 0° to the vertical with 3456 wires spaced 3 mm apart, and 2 planes where the ionization drifts passed and induces a signal at $\pm 60^\circ$ to the vertical each with 2400 wires also spaced 3 mm apart. Each plane has a spacing also of 3 mm from each other. The first two planes are the induction planes and the last is the collection. The 270 V/cm electric field of the TPC is created using 64 stainless steel tubes shaped into rectangles around the TPC and held in place by G10 to form a field cage. The cathode is charged at a high voltage of -70 kV and this voltage is stepped down across the field cage tubes using a voltage divider chain with an equivalent resistance of 240 M Ω between the tubes. The field cage tubes are separated by 4 cm from center to center. The electron drift distance is 2.5 m in the x direction with a drift time of 2.3 ms. Maintaining high charge yield is done by continuously recirculating and purifying the argon. The purity is monitored using MicroBooNE's light collection system. Another use of the light collection system is initial timing and drift coordinate of the interaction.

MicroBooNE's light collection system is a crucial part for 3D reconstruction of all particle interactions in the LArTPC. The initial interaction time, t_0 , and initial drift coordinate, x_0 , are not known from the TPC alone. For beam events, the accelerator clock is used to determine t_0 of the interaction and the x_0 can be inferred using drift time. Non-beam events, however, do not have this capability, which is why scintillation light from an interaction is used. The $\nu - Ar$ interaction produces scintillation light which is collected by photomultiplier tubes (PMTs) which allows the exact time, t_0 of the neutrino interaction to be determined. The scintillation light created propagates within nanoseconds to the light collection system compared to the milliseconds it takes the ionized electrons from the interaction to reach the anode wire planes. Therefore we can precisely know where along the drift direction the particle interaction first took place. The scintillation light is also localized, so combining the PMT information with the wire plane information allows for cosmic background rejection happening outside the beam timing window.

The light collection system is made up of 32 Hamamatsu R5912-02mod cryogenic PMTs with a diameter of 8-inches. The PMTs are located behind the 3 wire anode planes and provides 0.85% photocathode coverage. Each PMT has an acrylic plate mounted in front of it that is coated with a wave-length shifting material called TPB.

The acrylic plates take in the scintillation light, at 128 nm, and re-emits it visible wavelengths visible to the PMTs, with a peak at 425 nm.

Both the light collection system and the TPC create analog signal that is read out and digitized by the electronics system. The process requires amplification and shaping of the signal which then is goes to the data aquisition (DAQ) software for writing of the digitized data to disk. The anode plane wires are connected to detector specific circuit boards (ASICS) that are submerged and operate inside the liquid argon volume. These ASICS send amplified signal to 11 feed-throughs where further amplification of the signal happens outside the cryostat. The signal is received by custom LArTPC readout modules distributed over nine readout crates which do the digitization. The TPC wires are digitized at 16 MHz then downsampled to 2 MHz. The TPC system reads out 4 frames of wire signal data per event, 1 frame before a trigger and 2 frames after the triggered frame. The four frames allows for identification of a neutrino interaction as well as cosmic background rejection. The process of digitization is similar for the light collection system. Each PMT signal undergoes a shaping with a 60 ns peaking time for digitization of multiple samples. The digitization occurs at 64 MHz but are not read out continuously during the TPC readout time. Only shaped PMT signal samples above a small threshold are read out and saved. Both the TPC and PMT readouts are initiated via triggers on a separate trigger board located in a warm electronics crate. The timing trigger is created by a timing signal from the BNB accelerator which is shaped and sent to the trigger board. The PMT trigger is generated when the PMT signal multiplicity is greater than 1 and the summed PMT pulse-height is more than 2 photo-electrons summed up over all PMT channels. When the trigger board gets both a timing trigger and a PMT trigger in coincidence, a BNB trigger is then generated by the board. This signal is then passed to all readout crates initiating the readout of data. The data is then sent to the DAQ software which then saves the data to disk into one event memory.

3.3. MicroBooNE's Physics Goals

3.3.1. The low-energy excess

The primary goal of the MicroBooNE experiment is to study and investigate the low-energy excess seen in MiniBooNE. MicroBooNE has the capability of confirming or

denying this excess as electrons or photons due to the detector being in the same beam, having a similar baseline, and lastly the detector being able to clearly distinguish between electrons and photons. LArTPCs use the topology of events as well as energy loss near the vertex to differentiate between single e^- tracks and photon-induced induced pair production $\gamma \rightarrow e^+ e^-$, which wasn't possible in MiniBooNE, a Cherenkov detector. This technique has been shown in the ArogoNeuT detector [?] and a side by side comparison of both event types in a LArTPC can be seen in figure ???. An excess in electrons would point towards new oscillation physics beyond the standard model, while photons would be within the standard model. MicroBooNE will observe a 4-5 σ signal.

3.3.2. Cross sections

MicroBooNE's neutrino cross-section program will be the first $\nu - Ar$ cross-section in the 1 GeV energy range and one of only a few cross-section measurements of $\nu - Ar$ in the world. MicroBooNE is also the first liquid argon detector to collect the highest statistics sample of neutrino interactions. Investigating final-state-interactions in the 1 GeV energy range provides information about short range nuclear correlations that affect the interpretations of neutrino oscillation experiment data.

3.3.3. Astroparticle physics

99% of energy leaving a supernova leaves in the form of neutrinos which can be seen by detectors on earth's surface. MicroBooNE will have a dedicated supernova data stream and a connection to the SuperNova Early Warning System [?] so when a nearby supernova explosion occurs, continuous data will be written for several hours that can be later analyzed for supernova neutrino events. This information coupled with information from other experiments can be used to better understand supernovae. [add infographic of supernova here](#)

3.3.4. Liquid argon detector development

The last physics goal for the MicroBooNE collaboration is to provide important information regarding LArTPC technology. Being the first in large scale LArTPCs in the US,

MicroBooNE will be able to provide improvements to High Voltage (HV) distribution, Noise Characterization [?], and Michel Electron Reconstruction [8].

Chapter 4.

The Booster Neutrino Beam

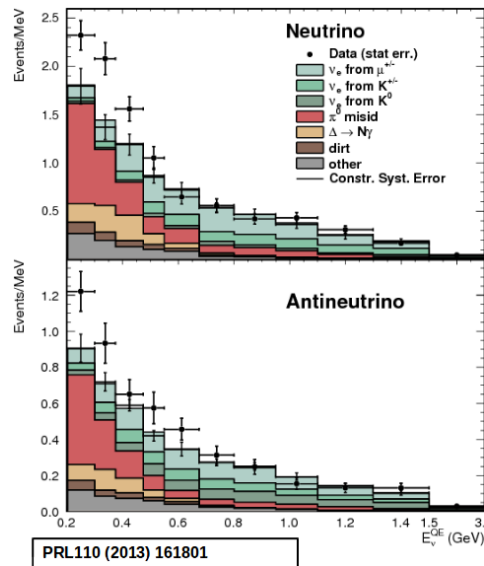
The MicroBooNE detector is stationed at Fermi National Accelerator Laboratory (FNAL) where it receives neutrinos from both the Booster Neutrino Beam (BNB) and Neutrinos from the Main Injector (NuMI) beams. MicroBooNE is on-axis for the BNB and off-axis by 135 mrad for NuMI. For the purpose of this analysis, only data from the BNB was used. This chapter will discuss how neutrinos are created using the BNB. How these neutrinos are produced as well as their flux through the MicroBooNE detector is necessary for any analysis because of the systematic uncertainties the beam introduces to a measurement.

4.1. Creating the Booster Neutrino Beam

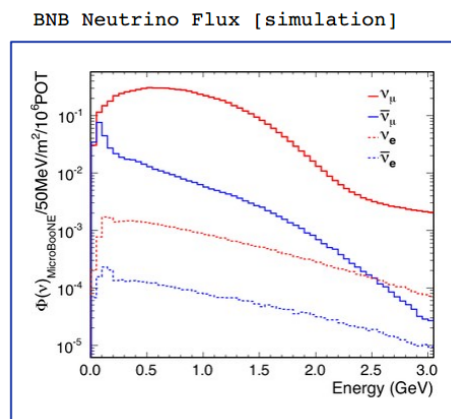
The BNB is a very pure ν_μ beam, with only 0.6% contamination from ν_e s. The energy also peaks around 700 MeV which is desired based on the probability of oscillation equation which depends on the the value of L/E , where L is the distance of the detector from the neutrino beam and E is the energy of the neutrino beam. L/E was chosen to increase the probability of seeing neutrino oscillations in the MiniBooNE Low Energy Excess (LEE) range based on the probability of oscillation equation, which is $P_{\nu_\mu \rightarrow \nu_e}(L, E) = \sin^2 2\theta \sin^2 \left(1.27 \Delta m^2 \frac{L}{E} \right)$. The BNB collides 8.9 GeV/c momentum protons from the FNAL booster synchrotron into a beryllium target which produces a high flux of neutrinos. The protons originate from H^2 gas molecules that are turned into H^- ions by a Cockroft-Walton generator shown in figure ???. The H^- initially are accelerated to 1MeV kinetic energy and are then passed to a linear accelerator using alternating electromagnetic fields to increase their energy to 400MeV. The ions are

stripped of electrons by passing them through a carbon foil. The protons are bunched into beam spills which contain 4×10^{12} protons in a $1.6 \mu\text{s}$ time window per spill. It's at this point that the protons are directed towards the beryllium target. The amount of protons directed towards the target (POT) is measured by two toroids upstream of the target with an error of 2%. Beam intensity, timing, width, position, and direction are monitored by beam position monitors, multi-wire chamber and resistive monitors. The beryllium target is 71.1 cm long, 1.7 proton interaction lengths, and is 0.51 cm in radius. The target is located inside a larger focusing electromagnet called the horn. The horn is an aluminum alloy pulsed toroidal electromagnet. The pulsed current peaks at 170 kA with a time-width of $143 \mu\text{s}$ which coincides with the protons arriving on the target. The current flows from the inner conductor to the outer conductor with a maximum magnetic field of 1.5 Tesla. The magnetic field focuses the charged secondary particles produced by the p-Be interactions. The direction of current can be switched to changed to polarity of the secondary particles being focused creating a beam of either primarily neutrinos, with positively charged secondary particles, or antineutrinos.

Further down the beamline is a concrete collimator which absorbs particles not necessary to the neutrino flux. The collimator is 214 cm long and 30 cm in radius. After the collimator comes a 45 meter long, 1 meter radius, air-filled cylindrical decay region which then ends in a beam-stop made of steam and concrete. The beam-stop contains an array of gas proportional counters to detect muons. **redadd beam diagram here**



(a) Low Energy excess seen in Mini-BooNE



(b) Energy spectrum of the Booster Neutrino Beam at Fermi National Laboratories

Figure 4.1.: 4.1b Flux of BNB at FNAL.

Chapter 5.

Neutrino Identification: Finding MicroBooNE's first Neutrinos

Chapter about your neutrinoID here.

More neutrinoID stuff.

Chapter 6.

CC-Inclusive Cross Section Selection Filter

One of the cross-section measurements MicroBooNE can make is an inclusive charged-current cross-section measurement (referred to as CC-inclusive). CC-inclusive events consist of a neutrino exchanging a W^\pm boson with an argon atom, producing a charged lepton and any number of other final state particles. In MicroBooNE's case, a CC-inclusive event will mostly have a defining muon track coming out of the vertex due to our neutrinos being predominately ν_μ s. A cross-section measurement is the energy dependent probability of $\nu - Ar$ interaction in the detector. Cross-sections however are independent of the intensity or focus of the particle beam so they can be compared among different experiments. A background for a CC-inclusive cross-section measurement are the neutral-current events that contain a pion. It is possible to have a neutral current interaction with a $\pi + p$ event signature that looks like a charged current $\mu + p$ event. Reconstruction tools implemented to date don't efficiently separate muons from pions. A common way to separate these two particles species is to implement a track length cut. On average, muons tend to have longer track lengths in LArTPCs so by requiring that the hypothesized lepton be above a threshold track length, it is possible to increase signal to background.

MicroBooNE requires fully automated event reconstruction and selection algorithms for use in the many physics measurements being worked on to date due to the large data rate MicroBooNE receives. Being able to automatically pluck out the neutrino interaction among a sea of cosmics proved to be challenging but was accomplished. MicroBooNE has developed two complementary and preliminary selection algorithms to select charged-current $\nu_\mu - Ar$ interactions. Both are fully automated

and cut based. The results below focus on the first selection and the “In-Progress” plots presented on the poster associated with this proceeding will focus on further improving this algorithm using Convolutional Neural Network (CNN) implementations. The full details can be found in MicroBooNE public note [?] and for more information of CNN implementation on MicroBooNE data refer to [?]. Selection I is based on cuts developed in a MC performance study described in [?]. It identifies the muon from a neutrino interaction without biasing towards track multiplicity. To combat cosmic and neutral current background, the analysis is strongly biased towards forward-going long tracks which are contained. This limits phase space and reduces acceptance.

The efficiency and purity are used as performance values of selection I. Efficiency is described as the number of selected true ν_μ CC events divided by the number of expected true ν_μ CC events. The purity is described as the number of selected true ν_μ CC events divided by the sum of itself and all the backgrounds. The efficiency of selection I is 12% and the purity is 39.7%. The poster related to this proceedings will focus on the last cut which requires the longest track to be longer than 75 cm. This cut has a passing rate of 30% w.r.t the previous cut and is implemented in part to separate charged-current events from neutral-current events that mimic our signal. Implementing a CNN for $\mu - \pi$ separation picks out differences in these two particles that are track range independent therefore eliminating the need for the 75 cm track length cut and increase efficiency and passing rate at low muon momentum. Figure 6.1a shows the track distribution of selection I and the lack of data below the 75 cm track length cut. Figure 6.1b shows the efficiency of selection I as a function of muon momentum. The selection begins with a cut that requires an optical flash greater than 50 photo electrons (PE) in the 1.6 μ s beam window. Next, two or more 3D reconstructed tracks must be within 5 cm from a 3D reconstructed vertex. The most forward going track vertex-track association is then selected for further cuts. The vertex from the chosen association must be in the fiducial volume, and the longest track from this association must be matched to a flash 80 cm in z. Lastly the longest track must be contained and longer than 75 cm.

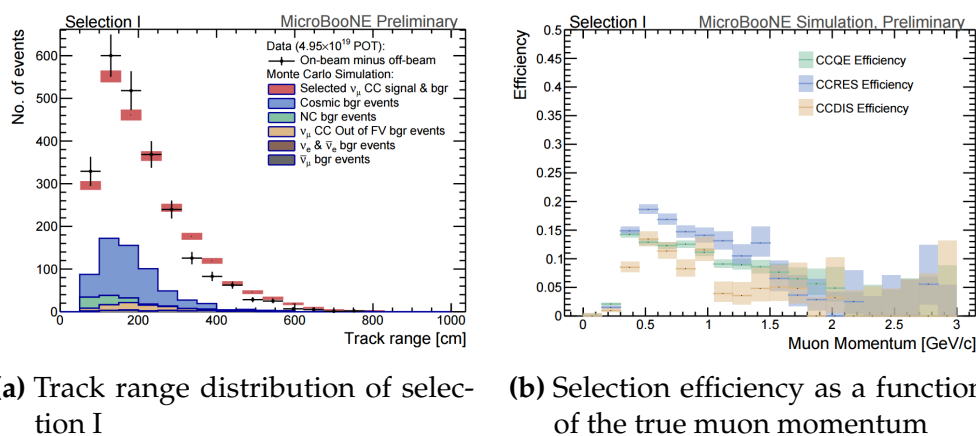


Figure 6.1: **6.1a** Track range distribution for selection I. The track range is defined as the 3D distance between the start and end of the muon candidate track. No data is shown below 75 cm due to the track length cut described previously. **6.1b** Efficiency of the selected events by process quasi-elastic (QE), resonant (RES), and deep-inelastic (DIS). Statistical uncertainty is shown in the bands and the distributions are a function of true muon momentum. The rise of the efficiency between 0 GeV and 0.5 GeV is due to the minimum track length cut and the decreasing efficiency for higher momentum tracks is caused by the containment requirement.

Chapter 7.

The importance of μ/π separation in MicroBooNE

μ/π separation chapter goes here.

More μ/π separation.

Chapter 8.

Convolutional Neural Networks

Image processing is processing of images by using any form of signal processing. Most image processing techniques treat an image like a 2-dimensional signal and apply standard signal processing techniques to it. Examples of image processing include Gaussian smoothing, edge detection, contouring and pattern recognition or high-level image processing like computer vision. By transforming each sample value for a single wire into a pixel value, it is possible to create a 2-D image from each LArTPC anode plane and hence apply image processing techniques. Gaussian smoothing is used to reduce the noise in an image. Edge detection algorithms look for discontinuities in an image and is the fundamental stage in pattern recognition or any higher level image processing, machine learning and computer vision due to the fact that it extracts the important features in an image. Once edge detection is applied to an image, a contouring algorithm can then be applied. A contour in image processing is an outline bounding an object of interest. A contour must be a closed line outlining in this case the edges found during edge detection. Once we have a bounded object, it is then possible to use these extracted features to train a computer vision algorithm like a Convolutional Neural Network (CNN) to learn that these features describe certain objects, and to then use these computer vision algorithms on random images.

When used for image recognition, convolutional neural networks consist of multiple layers of feature maps that extract different information on small portions of the input image. How many layers and feature maps is tunable to increase the matching process. The output of these collections are then tiled so that they overlap to gain a better representation of the original image and allow for translation. To truly understand CNNs, a breakdown of what convolution means with regards to imaging is necessary. Convolution of an image is using a map of some sort to extract features



Figure 8.1.: Applying a feature mask over a set of fashion items to extract necessary information for auto-encoding. Unnecessary information for example color or brand emblems are not saved. This feature map is an edge detection mask that leaves only shape information which helps to distinguish between different types of clothes.

from the input image by matrix multiplication. The map is multiplied to a small image patch and this is then saved. This is done until the whole image is processed and what is left is a feature map that has the important features extracted. An example of convolution for the process of object identification is shown in figure 8.1. In this figure you can see how an edge detection feature map is used to save only necessary information for recognizing different types of clothes. You can also see by having multiple feature maps you can get more detail or less detail from an image which can then simplify or complicate the object recognition task. Being able to distinguish between a shirt or a leg garment is as much information you want, having a feature map that extracts outline edge or shape information would be all that you need. But if instead you wanted to distinguish between a formal cocktail dress or a summer dress, more information would need to be saved equating to many more feature maps for one image. Rather than trying to come up with a scheme of feature maps to run over the image by hand, CNNs do this automatically. CNNs take input parameters, for example number of layers, number of units per layers, number of connections per unit, and uses these to create the feature maps. The layers build upon each-other, for example if we were creating a CNN for facial recognition the convolutional layers will start learning feature combinations off of the previous layers. The simple edges,

gradients, and corners of the first layers become things like eyes, noses, and hairs in later layers. This process is visualized in figure 8.2

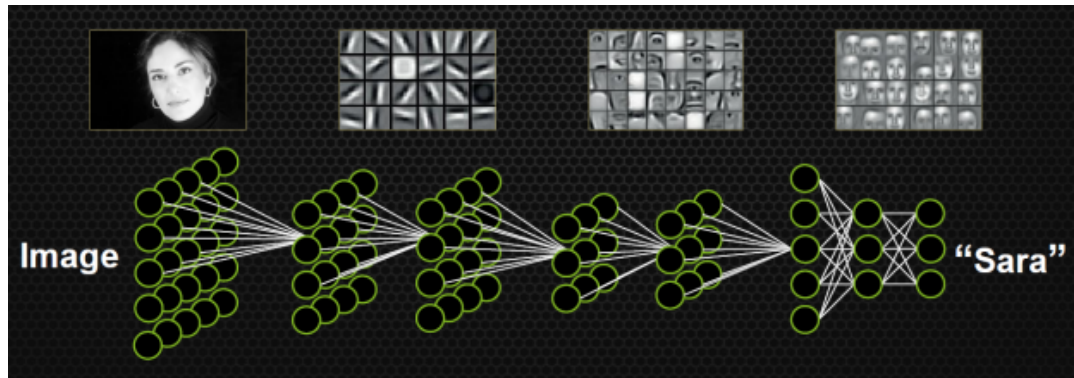


Figure 8.2.: Pictorial Representation of Convolutional Neural Networks as well as a visual representation on CNN's complexity of layer feature extraction

Chapter 9.

Hardware Frameworks

Chapter about different frameworks used/timing on each setup.

9.1. Syracuse CPU Machine setup

9.2. Syracuse University GPU Cluster Setup

...

Chapter 10.

Using Convolutional Neural Networks to separate μ' s from π' s

The work shown in these next sections are based on the previous work done described in [?]. That CNN (now referred to as CNN1075) was trained using single generated isotropic muons and pions from 0-2 GeV energy range. 1,075 muons and pions were used to train the network and 1,075 μ/π were used as a validation set. The accuracy is how well CNN1075 is doing by epoch and was 74.5%. The loss is gradient descent or minimization of the error of the weights and biases used in each neuron of each layer of CNN1075 and was 58% with a trend sloping downwards on the loss curve as well as a trend sloping upward in the accuracy curve. Due to the depth of the neural network framework, it was necessary to train with a larger dataset and for more epochs, however, the downward slope of the loss curve is an indication that once trained for longer with a higher training sample, neural networks can be used for μ/π separation. Updates in the image making and downsampling algorithm were made to fix issues that arose in CNN1075.

10.1. Image Making Scheme

The μ/π image dataset used to train and test the second CNN (now referred to as CNN10000) was created using single generated isotropic muons and pions from 0-2 GeV energy range. 10,000 muons and 10,000 pions were used for training and testing split 50%. The images were created based on wire number and time tick in the collection plane. Uboonecode v06_23_00 was used instead of v05_08_00 which was

used previously. The wire signal was the raw ADC value after noise filtering. Each collection plane grayscale image was 3456x1280x1 where 5 time ticks were pooled into 1 bin which is different than the previous dataset and was implemented due to the fact that the time ticks of an event went from 9400 to 6400 with the change of uboonecode version. The grayscale color standard is 8bit therefore the ADC value of wire and time tick was also downsampled due to the 12bit ADC value MicroBooNE has. To do this, the highest ADC pixel in the image was found and then this was divided by the rest placing all pixel values between 0-1. From there, all pixel values are then multiplied by 255. All images were made using a LArSoft module. Once the images were created, using an image manipulation framework called OpenCV images were read into a numpy array and cropped to the region of interest by only keeping rows and columns where all ADC values are higher than 0 and then resized it to 224x224 using OpenCV's resize function. This downsampling of ADC values creates a problem of information loss for example, a proton which is highly ionizing will have the same brightness as a minimum ionizing muon by virtue of how the images are created. Creating images that thoroughly depict the ADC scale for use in dE/dx particle identification has been implemented and retraining of CNN is underway. Issues that arose in CNN1075 that were fixed in CNN10000 include zero-padding images in X and Y that are smaller than 224X224 to eliminate over-zooming effect and fixing a bug that shifted pixels separated by a dead-wire region.

Images were also made from events that passed the cc-inclusive selection 1 filter right before the 75 cm track length cut and were classified using the CNN10000. The dataset used to create these images is the same one used in [?], prodgenie_bnb_nu_cosmic_uboone_mc. These images were created using information from the track candidate that passed the filter. Only wire number and time ticks associated to the track candidate were drawn on the image to mimic a single particle generated image. These images were then classified using CNN10000. Two approaches were taken in making these images. The first was using the image normalization above where the maximum pixel in each image is used as a normalization constant to get all pixels between 0-1 then multiply all pixels by 255. As described above, this is the incorrect way to normalize; it should be normalized by dataset not by event, which is the second way the images were created. The results of CNN10000 performance are shown in section 10.2.

10.2. Convolutional Neural Network Training

The hyperparameters used for CNN10000 are shown. The batch size for the training and testing as well as the test iter were chosen to encompass the whole training/testing image set when doing accuracy/loss calculations. To do this, multiplying the test iter by the test batch size give you the amount of images used when calculating accuracy/loss curves. For reference, the accuracy and loss are defined as well.

- train_batch_size: 100
- test_batch_size: 100
- test_iter: 100
- test_interval: 100
- base_lr: 0.001
- lr_policy: "step"
- gamma: 0.1
- stepsize: 1000
- display: 100
- max_iter: 10000
- momentum: 0.99
- weight_decay: 0.0005
- snapshot: 100
- Accuracy: How often the CNN predicts the truth over total number of images
- Loss: Error between truth and prediction. Minimize loss by gradient descent to update weights and biases of CNN

The same architecure that was used to train CNN1075 was employed on CNN10000, Imagenet. Caffe [?] was the software package used for both CNNs. The differences include batch size and test_iter and momentum to account for the larger dataset. Both CNNs were trained on a CPU machine, Syracuse01. Further training will be done on a GPU cluster stationed at Syracuse University. Figure 10.1 shows the loss and

accuracy of CNN10000. There is around a 10% increase in accuracy from CNN1075 to CNN10000, 85%, and around a 20% decrease in loss, 36%.

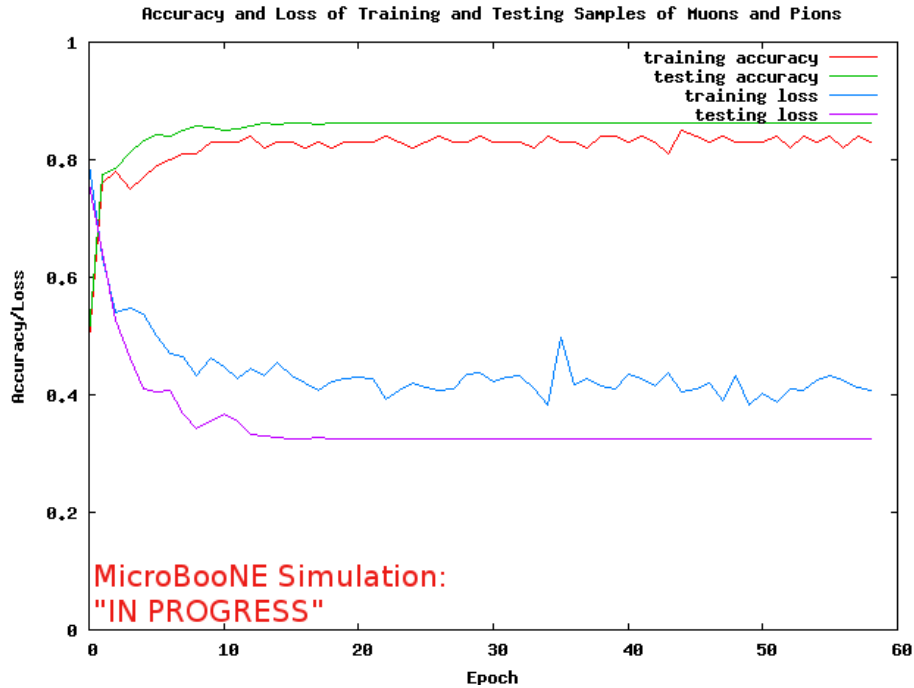


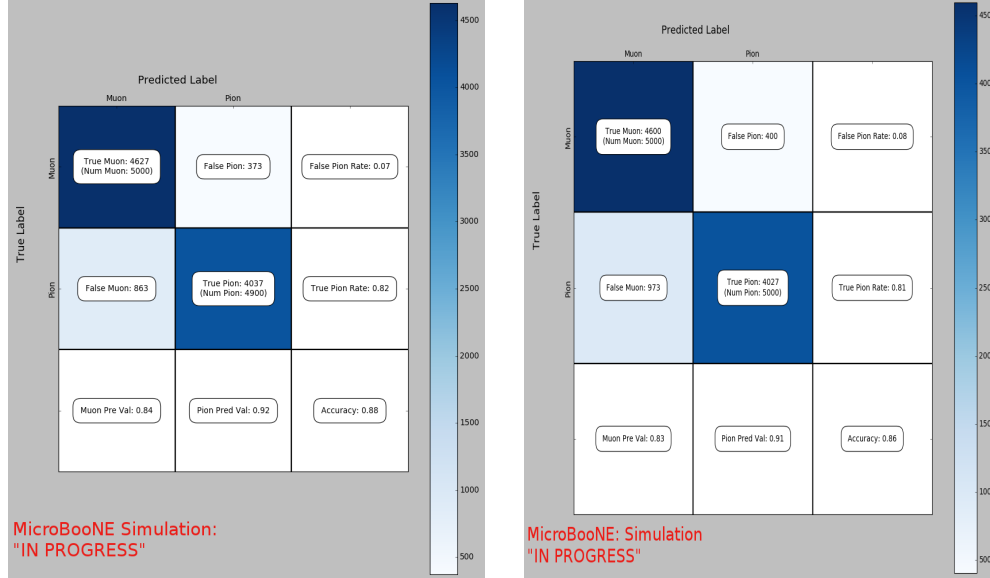
Figure 10.1.: Accuracy vs. Loss of ImageNet 2-output μ/π sample consisting of 10000 images each.

Figure 10.2 show a breakdown of μ/π separation for CNN10000. It also shows the network is not being overtrained due to the Accuracy of both the training and testing datasets being within .01% of eachother. The CNN is doing a very good job of classifying true muons as muons, and our loss increase from CNN1075 is due to the increase in accuratly classifying pions as pions.

10.3. Classification of MC data using Selection I

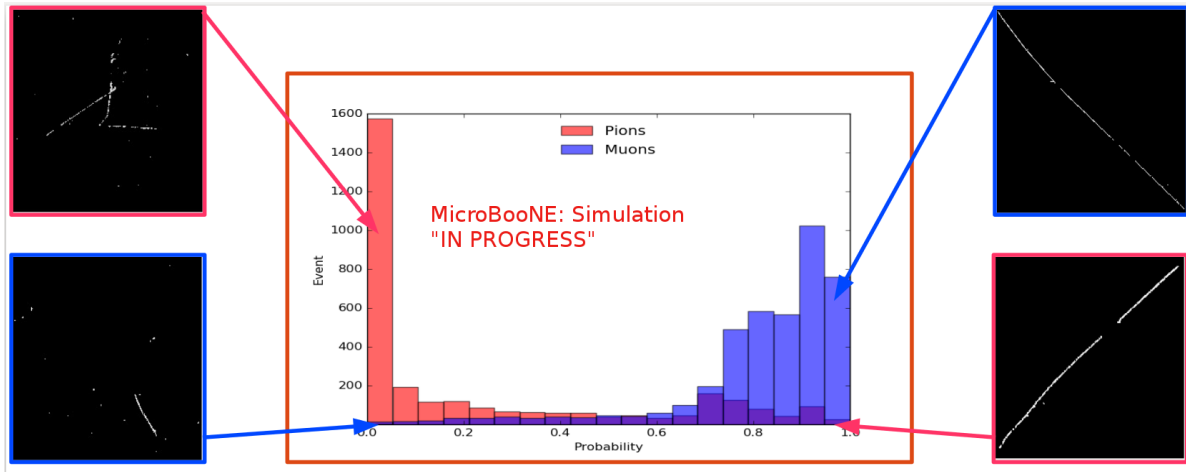
Original CC-Inclusive Filter

The next step that was taken was to use CNN10000 to classify track candidate images that were identified by the selection I original cc-inclusive filter described in [?]. Passing rates for each cut in cc-inclusive filter are show in figure 10.3. For the incorrect image making normalization dataset, out of 188,880 events, 7438 passed the cut right before 75 cm track length cut which is 3.9% of total data. Discrepancies in passing rates



(a) Confusion Matrix showing Accuracy of CNN using training data

(b) Confusion Matrix showing Accuracy of CNN using testing data



(c) Probability plot of muons and pions from testing set. Images surrounding histogram are a random event from lowest bin and highest bin for each particle.

Figure 10.2.: Description of confusion matrix variables: False pion rate = $false\pi / total\pi$ True pion rate = $true\pi / total\pi$ Accuracy = $(true\pi rate + true\mu rate) / 2$ Pion prediction value = $true\pi / (true\pi + false\pi)$ Muon prediction value = $true\mu / (true\mu + false\mu)$

10.2c The probability plot includes muons and pions that are classified as primary particles.

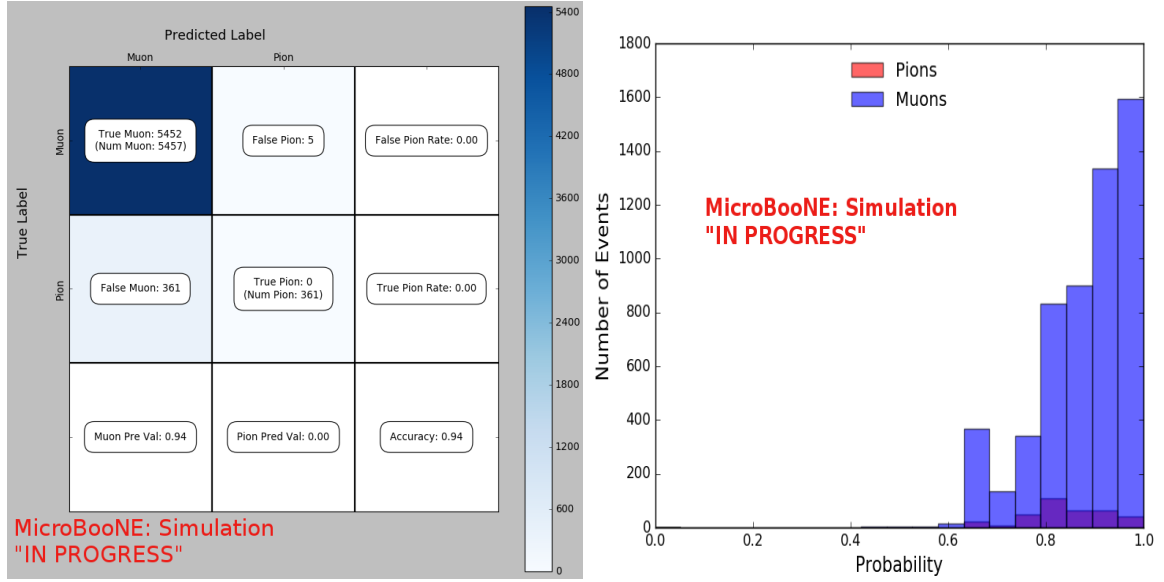
Table 3: **Selection I: Original** The table shows passing rates for the above described event selection. Numbers are absolute event counts and Cosmic background is not scaled appropriately. The BNB+Cosmic sample contains all events, not just ν_μ CC inclusive. The selected events are further broken up in the following subsection. The numbers in brackets give the passing rate wrt the step before (first percentage) and wrt the generated events (second percentage). In the BNB+Cosmic MC Truth column shows how many true ν_μ CC inclusive events (in FV) are left in the sample. This number includes possible mis-identifications where a cosmic track is picked by the selection instead of the neutrino interaction in the same event. The cosmic only sample has low statistics, but please note that it is not used in any plots, it is just for illustrating the cut efficiency. The last column Signal:Cosmic only gives an estimate of the ν_μ CC events wrt the cosmic only background at each step. For this number, the cosmic background has been scaled as described in chapter 2. Note that this numbers is not a purity, since other backgrounds can't be determined at this step.

	BNB + Cosmic		Cosmic only		Signal: Cosmic only
	Selection	MC-Truth			
Generated events	191362	45273	4804		1:22
≥ 1 flash with ≥ 50 PE	136219 (71%/71%)	44002 (97%/97%)	2979 (62%/62%)		1:14
≥ 1 vertex in FV	131170 (96%/69%)	43794 (99%/97%)	2805 (94%/58%)		1:13
≥ 1 track within 5 cm of vertex	129784 (99%/68%)	43689 (99%/97%)	2756 (98%/58%)		1:13
flash matching of longest track	44775 (34%/23%)	23647 (54%/52%)	647 (23%/13%)		1:5.7
track containment	10114 (23%/5.3%)	6882 (29%/15%)	61 (9.4%/1.3%)		1:1.9
track ≥ 75 cm	7358 (73%/3.8%)	5801 (84%/13%)	31 (51%/0.6%)		1:1.1

Figure 10.3.: Snapshot of passing rates of Selection I from CC-Inclusive Filter

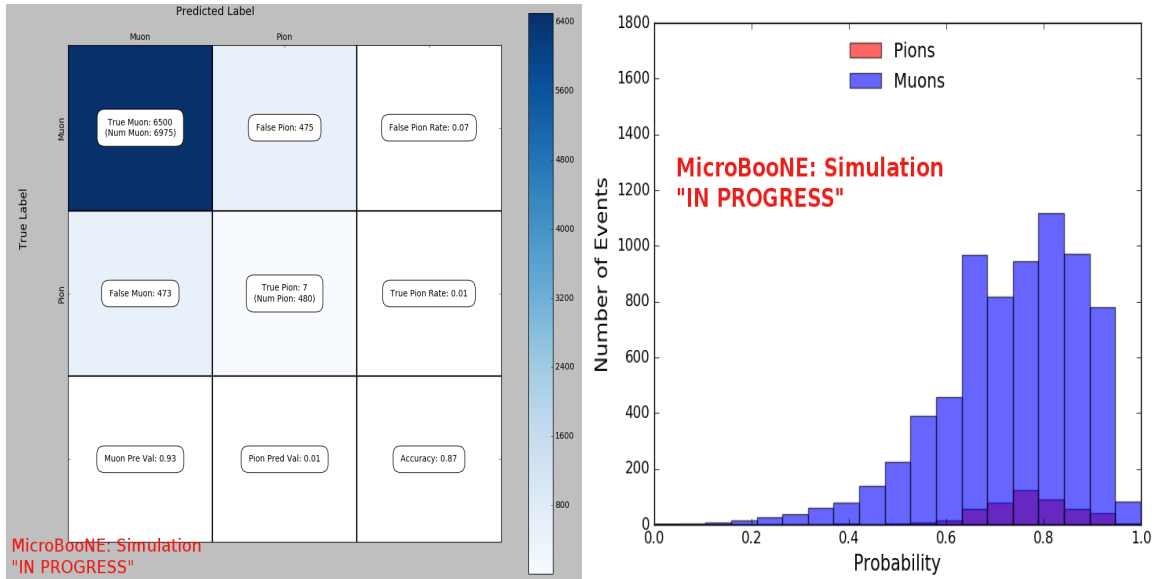
are due to grid submission issues, however, this dataset is used to check if changes in image making normalization affects μ/π separation probability due to CNN10000 being trained with incorrectly image making normalized data. For the second dataset with correct image making normalization, out of 188,880 events, 9552 events passed the cut right before the 75 cm track length cut which is 5.1% passing rate and is comparable to figure 10.3. In time cosmics were also run over for efficiency and purity calculations. Out of 14395 in time cosmic events, 175 passed the cut right before the 75 cm track length cut which is a passing rate of 1.2% compared to 1.3% shown in figure 10.3.

Figures 10.4a, 10.4b, 10.4c and 10.4d show the accuracy and μ/π separation of both the correct and incorrect normalized images. The confusion matrices are only composed of μ/π data. Other particles passed the cc-inclusive filter before the 75 cm track length cut and were all mis-id'ed as muons. Since CNN10000 has not seen any particles other than muons and pions, it makes sense that those get mis-id'ed. Figures 10.4b and 10.4d don't have μ/π separation comparable to 10.2c, but 10.4b does skew to higher probabilities compared to 10.4d. This is to be expected and further work on quantifying the performance of CNN10000 should use the incorrect image making normalization. It is also expected that the separation isn't as defined as the testing dataset for CNN10000. CNN10000 was trained and tested using single particle muons and pions and the track candidate dataset come from BNB+Cosmic events, not to mentions all track candidates have passed the cc-inclusive filter that



(a) Confusion Matrix showing Accuracy of CNN using data with wrong normalization

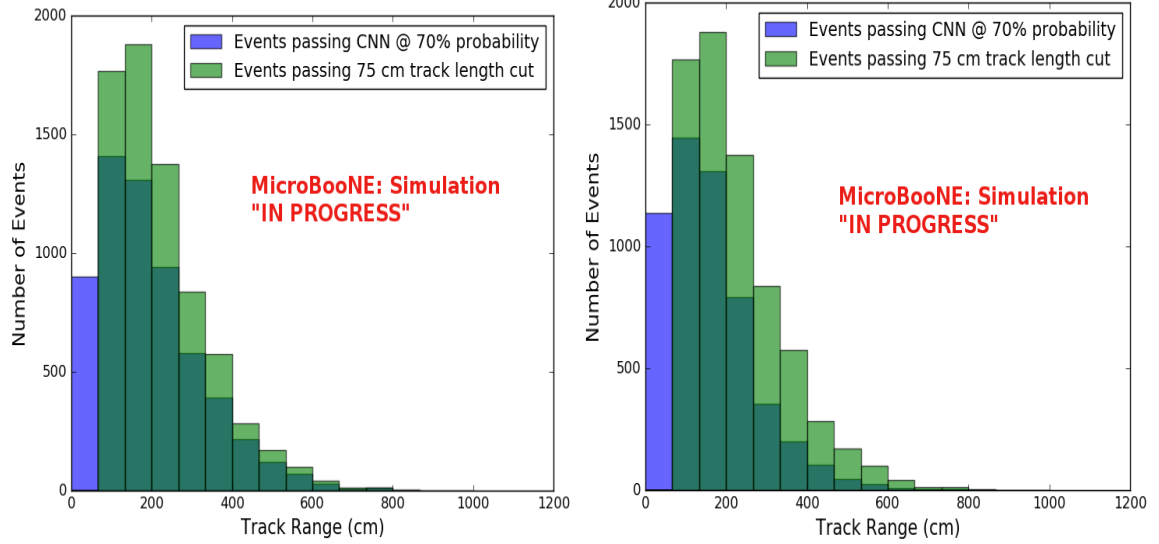
(b) Probability plot showing μ/π separation of CNN using wrong normalization



(c) Confusion Matrix showing Accuracy of CNN using data with correct normalization

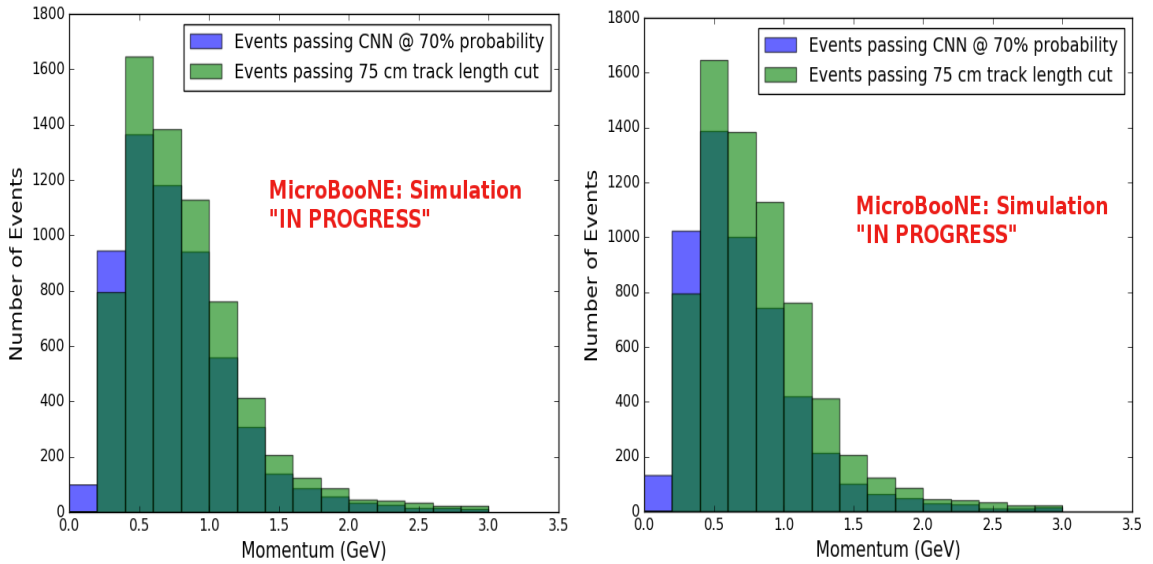
(d) Probability plot showing μ/π separation of CNN using correct normalization

Figure 10.4.: Results of CNN10000 classification of track candidate images output from cc-inclusive filter.



(a) Track range distribution of events from Selection I Original passing CNN with 70% accuracy using image data with wrong normilazion

(b) Track range distribution of events from Selection I Original passing CNN with 70% accuracy using image data with correct normilazion



(c) Momentum distribution of events from Selection I Original passing CNN with 70% accuracy using image data with wrong normilazion

(d) Momentum distribution of events from Selection I Original passing CNN with 70% accuracy using image data with correct normilazion

Figure 10.5: CNN10000 distributions of track candidate images output from Selection I Original cc-inclusive filter with different image data normalizations

tags "muon-like" tracks therefore the pions in this sample look much closer in muon topology than the network has seen. Also, these images were made from wire and time ticks associated to hits from the track candidate that passed the cc-inclusive filter. This is different from the training images where a bounding box was drawn over the total μ or π interaction. Spurious energy deposition from a $\pi - Ar$ interaction is most likely not included in the BNB+Cosmic images due to the tracking algorithm. To remedy this, the neural network needs to see more "muon-like" pions and muons and pions from a neutrino interaction passing the cc-inclusive filter as well as a larger particle variety including protons, photons and electrons. Although μ/π separation is lacking, CNN10000 does an excellent job of classifying muons and using higher CNN probability can increase purity. Figures 10.5a, 10.5b, 10.5c and 10.5d show the track and momentum distributions for these two datasets. In both sets you have an increase in data in the bin below 75 cm and at bins below 0.5 GeV. These distributions were made with events classified with 70% probability of being a muon regardless of true particle type.

10.4. Classification of MC data using Selection I Modified CC-Inclusive Filter

Table 5: **Selection I: Modified** The table shows passing rates for the above described event selection. Numbers are absolute event counts and Cosmic background is not scaled appropriately. The BNB+Cosmic sample contains all events, not just ν_μ CC inclusive. The selected events are further broken up in the following subsection. The numbers in brackets give the passing rate wrt the step before (first percentage) and wrt the generated events (second percentage). In the BNB+Cosmic Mc Truth column shows how many true ν_μ CC inclusive events (in FV) are left in the sample. This number includes possible mis-identifications where a cosmic track is picked by the selection instead of the neutrino interaction in the same event. The cosmic only sample has low statistics, but please note that it is not used in any plots, it is just for illustrating the cut efficiency. The last column Signal:Cosmic only gives an estimate of the ν_μ CC events wrt the cosmic only background at each step. For this number, the cosmic background has been scaled as described in chapter 2. Note that this numbers is not a purity, since other backgrounds can't be determined at this step.

	BNB + Cosmic		Cosmic only		Signal:
	Selection	MC-Truth			Cosmic only
Generated events	191362	45273	4804		1:22
≥ 1 flash with ≥ 50 PE	136219 (71%/71%)	44002 (97%/97%)	2979 (62%/62%)		1:14
≥ 1 track within 5 cm of vertex	135830 (99%/71%)	43974 (99%/97%)	2975 (99%/62%)		1:14
vertex candidate in FV	79112 (58%/41%)	34891 (79%/77%)	1482 (50%/31%)		1:8.9
flash matching of longest track	40267 (51%/21%)	25891 (74%/57%)	340 (23%/7.1%)		1:2.8
track containment	19391 (48%/10%)	11693 (45%/26%)	129 (38%/2.7%)		1:2.3
track ≥ 75 cm	6920 (36%/3.6%)	5780 (49%/13%)	17 (13%/0.4%)		1:0.6

Figure 10.6.: Snapshot of passing rates of all cuts from Selection I Modified cc-inclusive filter

CNN10000 was also used to classify track candidate images that were identified by the selection I modified cc-inclusive filter described in [?]. Passing rates for each cut in this filter are shown in figure 10.6. As seen in section 10.3, wrong image normalization had a higher muon classification probability so all work done using selection I modified cc-inclusive filter was done using this normalization. Out of 188,880 events, 19,112 passed the cut right before the 75 cm track length cut which is a 10.1% passing rate and comparable to the 10% passing rate shown in figure 10.6. In time cosmics were also run over, out of 14,606 in time cosmics events, 302 passed the cut right before the 75 cm track length cut which is a 2.1% passing rate comparable to the 2.7% passing rate in the cc-inclusive tech-note. Figures 10.7a and 10.7b show the accuracy and μ/π separation. Both plots are only composed of muons and pions and like selection I original data, all other particles were id'ed as muons. Also like selection I original data, muons are being identified at a very high rate. Figure 10.8a shows the track range distributions of all events from selection I modified being classified by the CNN as a muon with a probability of 70% regardless of true particle type. We get entries for the CNN curve in the lowest bin and none for the 75 cm curve. To see how many true CC events were identified by CNN10000 breaking down figure 10.8a by event type was necessary. Figures 10.8b and 10.8c show track range distributions separated by signal and various backgrounds. Particle type was not taken into consideration in these plots so true CC event images can be any track candidate particle passing selection I modified cut right before track length cut including pions and protons.

To gain an even deeper understanding on how CNN10000 is performing, plotting these distributions with only muons and pions was done due to the fact that CNN10000 was trained with only those particles for μ/π separation. Figures 10.8d-10.9d show the stacked histograms of signal and background of the track range distributions with varying CNN probabilities starting from 70% and ending at 90% probability. With higher probabilities we get a purer sample in the lower bin but we end up losing events as well. Momentum distributions for all signal/background events are shown in figure 10.10.

Another check was to see if any true CC pions were passing through the cut right before the 75 cm track length cut. Figure 10.11 shows the comparison of the stacked track range distribution with only true CC muon signal versus the stacked distribution with true CC muons and pions signal. As you can see, we gain more events when plotting CC events with a particle type of either muons or pions due to the CNN classifying all pions in this dataset as muons. This is an interesting scenario and a

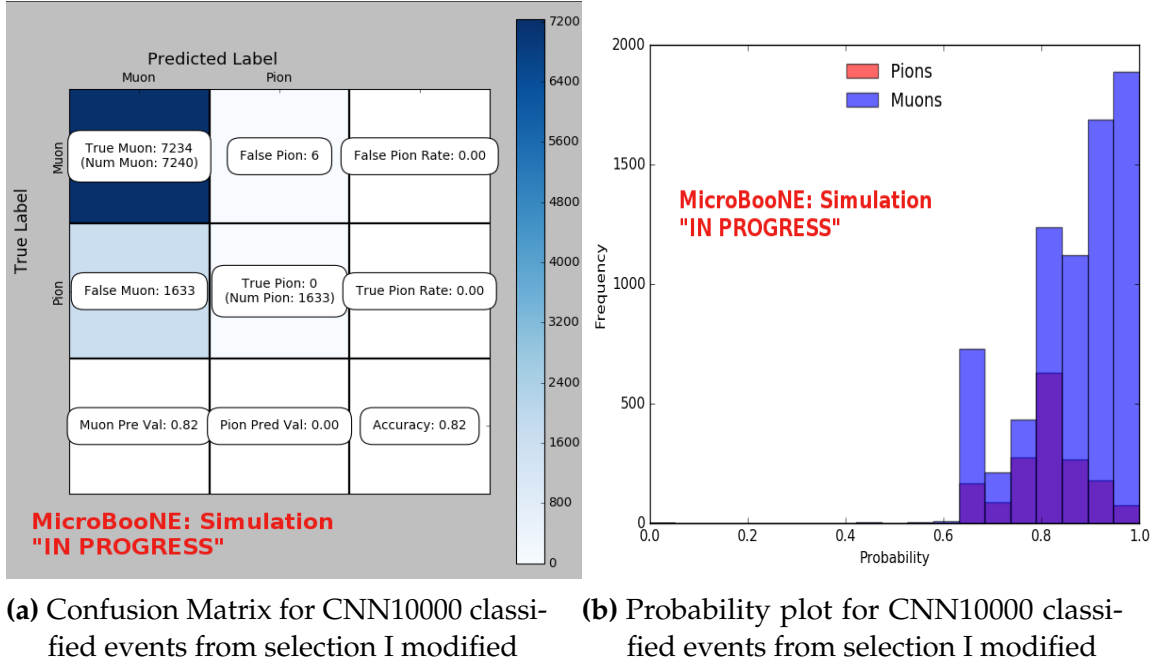
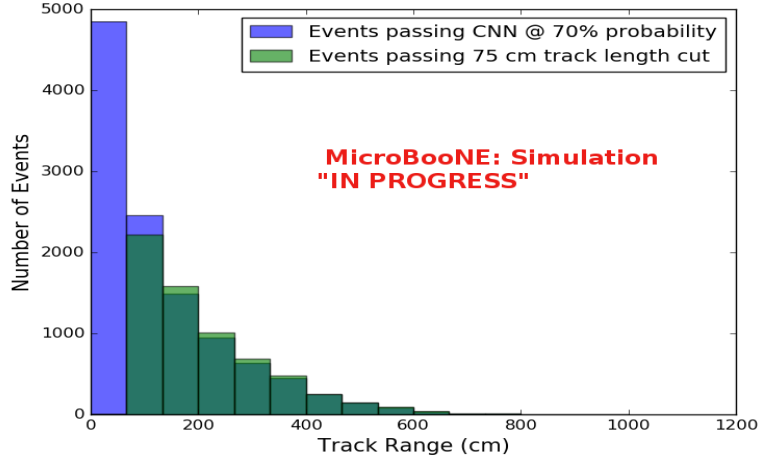
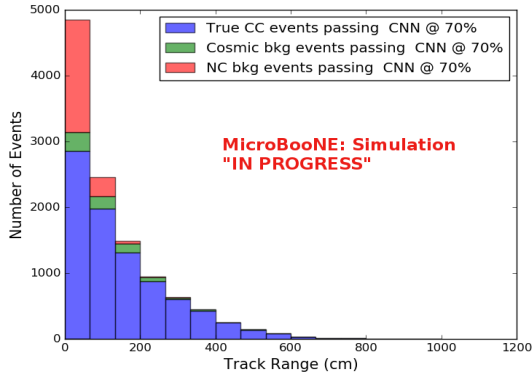


Figure 10.7.: Confusion matrix and probability plot of events passing selection I modified cc-inclusive cuts right before 75cm track length cut

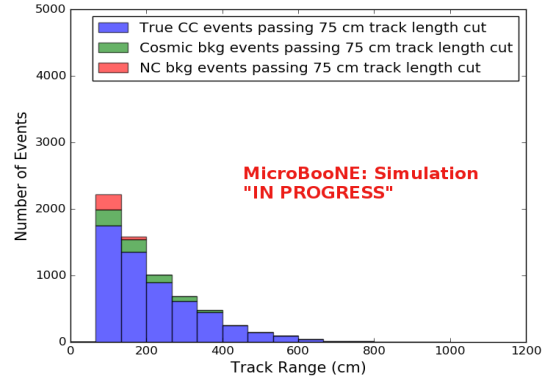
sample of topologies of these images are represented in figure 10.12, at least 3 tracks are coming out of the vertex for these types of events. With the 75 cm track length cut, the selection is cutting event topologies like this where the pion is the tagged track candidate. Figure 10.12a has a defined longer muon track, but because of dead wires through the track, the reconstructed range is 1. less than 75 cm and 2. shorter than the reconstructed pion whose length is also less than 75 cm. This is a very interesting event, but because of issues with the tracking algorithm, the 75 cm cut would get rid of this event. The CNN was able to recover this event only because it has classified all pions as muons. Figure 10.12b shows the second case to think about, the pion, while still less than 75 cm has a reconstructed track length longer than the muon. Again, the CNN recovered this event due to pions being classified as muons. Lastly, figure 10.12c shows a pion with a reconstructed track length greater than 75 cm and the muon. These three cases show that a broader question must be asked when training the network other than is it a muon or pion. There are different routes to recover interesting events like these. One route is to ask the network “Is it a CC event or is it an NC event?” and obtain an image dataset consisting of whole CC/NC events that will train the network to answer this question. The other route is to ask the network “Is this a $\mu/\pi/p/$ from a CC event or NC event and obtain an image dataset consisting



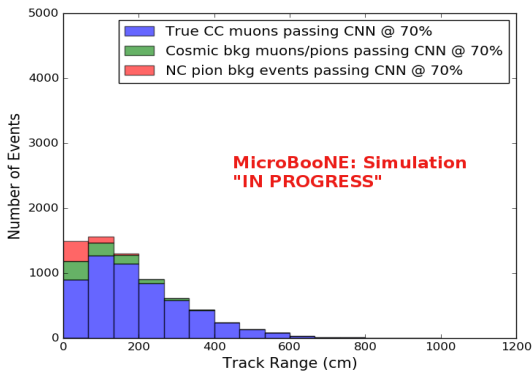
(a) Track range distribution of events from Selection I Modified passing CNN with 70% accuracy



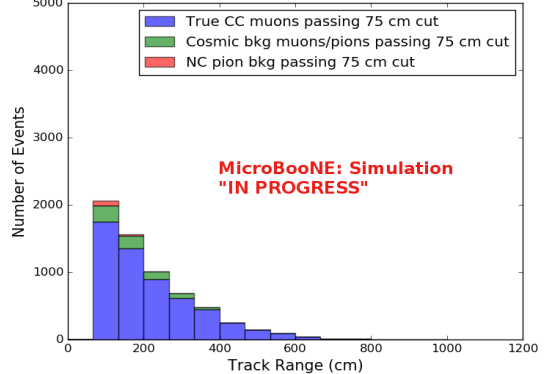
(b) Stacked signal and background track range distributions from Selection I Modified passing CNN with 70% accuracy



(c) Stacked signal and background track range distributions from Selection I Modified passing 75 cm track length cut

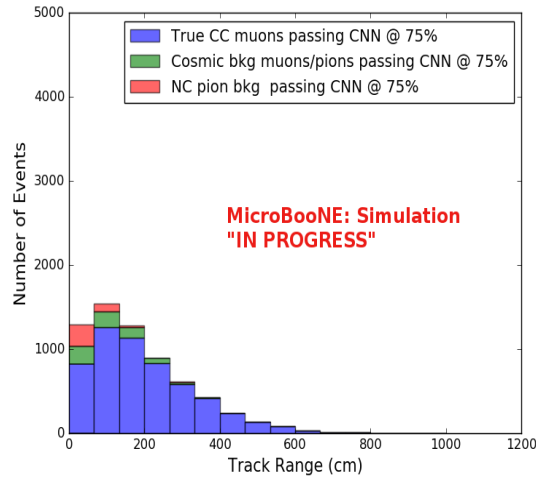


(d) Stacked signal muons and background muons/pions of track range distributions from Selection I Modified passing CNN with 70% accuracy

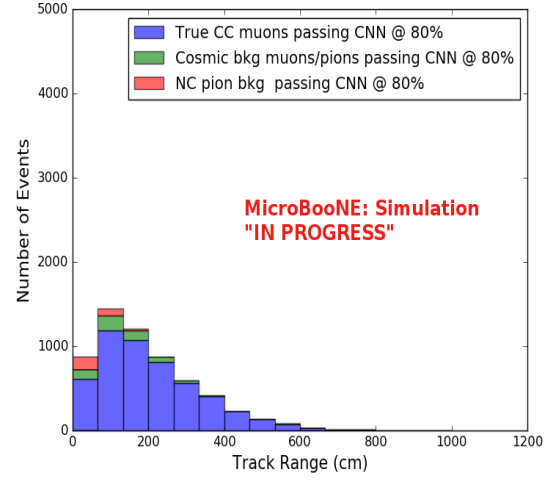


(e) Stacked signal muons and background muons/pions of track range distributions from Selection I Modified passing 75 cm track length cut

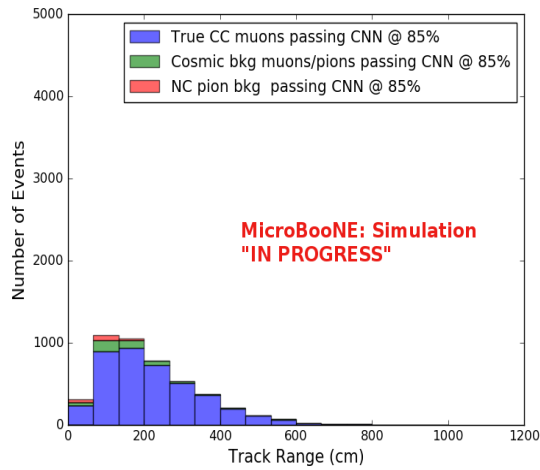
Figure 10.8.: CNN10000 distributions of track candidate images output from Selection I Modified cc-inclusive filter



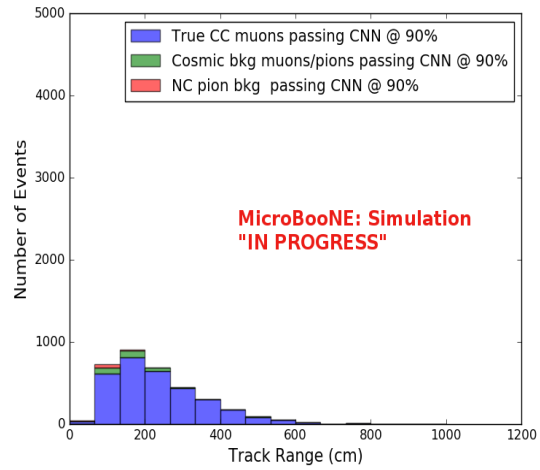
(a) Stacked signal muons and background muons/pions of track range distributions from Selection I Modified passing CNN with 75% accuracy



(b) Stacked signal muons and background muons/pions of track range distributions from Selection I Modified passing CNN with 80% accuracy

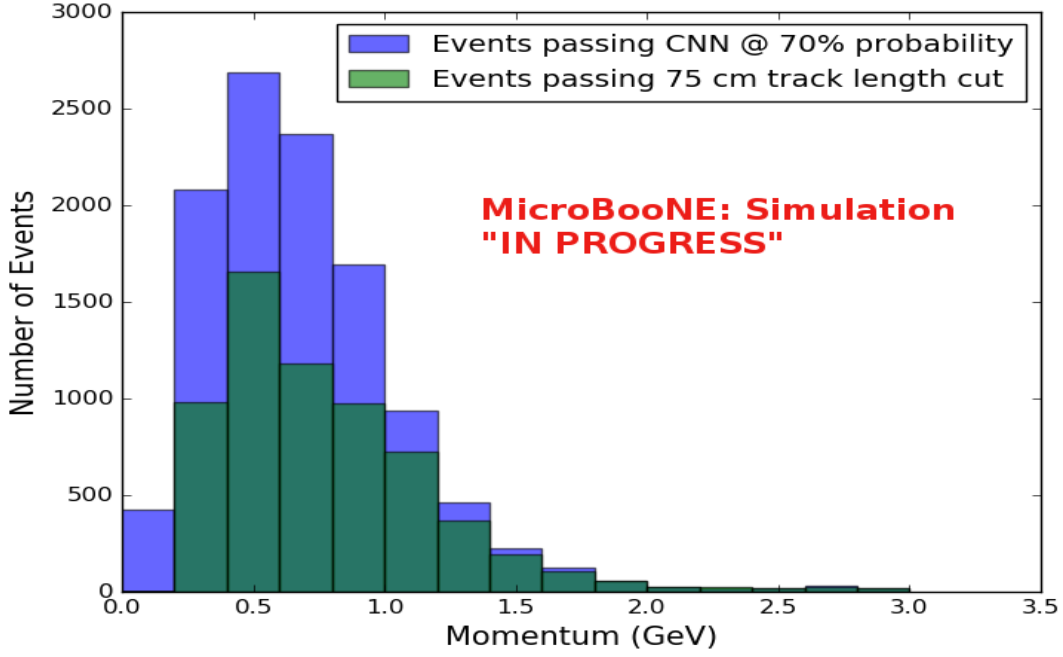


(c) Stacked signal muons and background muons/pions of track range distributions from Selection I Modified passing CNN with 85% accuracy

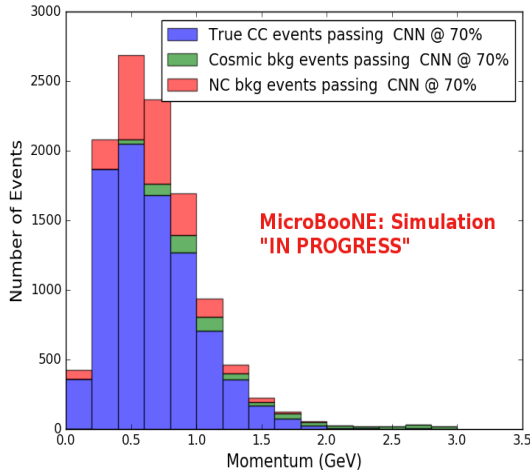


(d) Stacked signal muons and background muons/pions of track range distributions from Selection I Modified passing CNN with 90% accuracy

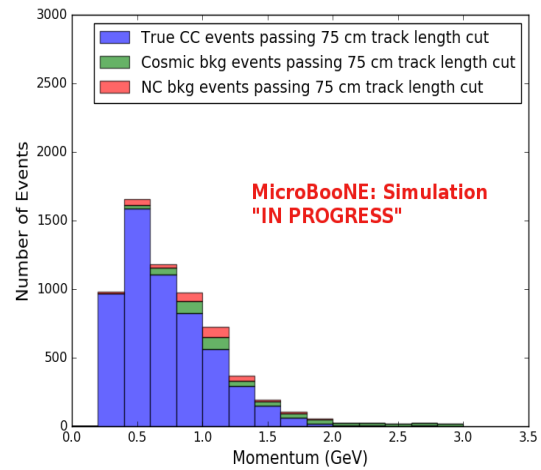
Figure 10.9.: CNN10000 stacked signal/background track range distributions of track candidate images output from Selection I Modified cc-inclusive filter



(a) Momentum distribution of events from Selection I Modified passing CNN with 70% accuracy



(b) Stacked signal and background momentum distributions from Selection I Modified passing CNN with 70% accuracy



(c) Stacked signal and background momentum distributions from Selection I Modified passing 75 cm track length cut

Figure 10.10.: CNN10000 momentum distributions of track candidate images output from Selection I Modified cc-inclusive filter

of primary particles from a CC/NC event. Both these paths will be explored in future work.

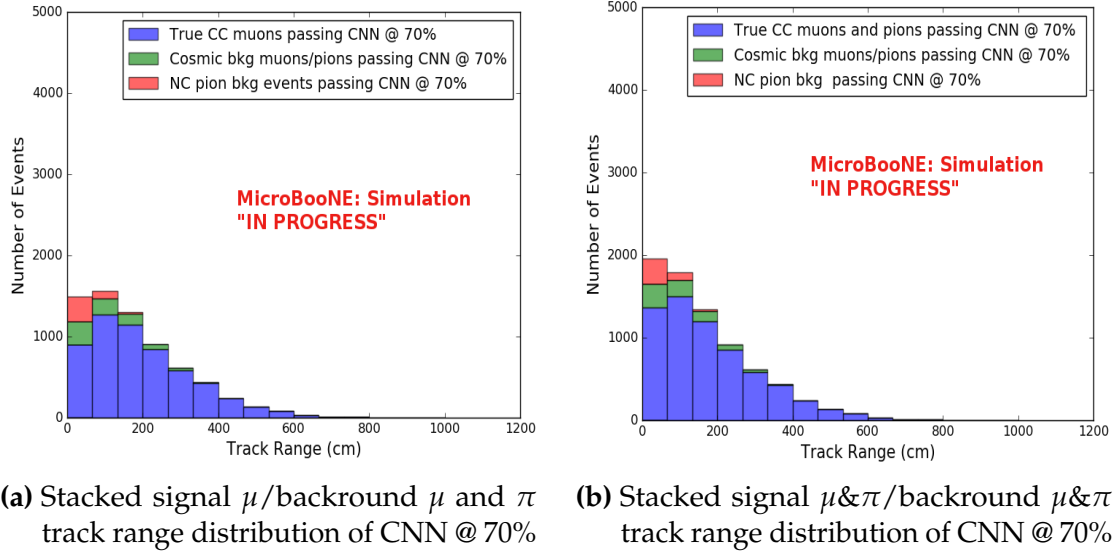


Figure 10.11.: Track distribution comparisons of true CC muons plotted vs true CC muons and pions plotted



(a) Pion reconstructed track range is less than 75 cm and longer than muon track due to dead wires

(b) Pion reconstructed track range is less than 75 cm and larger than muon reconstructed track

(c) Pion reconstructed track range is greater than 75 cm and larger than muon reconstructed track

Figure 10.12.: Images of true CC events where the pion was the tagged track candidate

		BNB + Cosmics		Cosmic Only	Signal: Cosmic Only
		Selection	MC Truth		
75 cm Cut passing rates	Generated Events	191362	45723	4804	1:22
	Track Containment	19391 (48%/10%)	11693 (45%/26%)	129 (38%/2.7%)	1:2.3
	track ≥ 75 cm	6920 (36%/3.6%)	5780 (49%/13%)	17 (13%/0.4%)	1:0.6
CNN passing rates	Generated Events	188880	44689	14606	1:21
	Track Containment	19112 (/10%)	11554 (/26%)	302 (/2.1%)	1:1.73
	CNN cut @ 70% Probability	16502 (86%/8.7%)	10605 (92%/23%)	205 (68%/14%)	1:1.28
	CNN cut @ 83% Probability	7511 (46%/4.0%)	6142 (58%/14%)	32 (16%/0.2%)	1:0.4

Table 10.1.: Comparing passing rates of CNN at different probabilities versus 75 cm track length cut: Numbers are absolute event counts and Cosmic background is not scaled appropriately. The BNB+Cosmic sample contains all events. The numbers in brackets give the passing rate wrt the step before (first percentage) and wrt the generated events (second percentage). In the BNB+Cosmic MC Truth column shows how many true ν_μ CC-inclusive events (in FV) are left in the sample. This number includes possible mis-identifications where a cosmic track is picked by the selection instead of the neutrino interaction in the same event. The CNN MC True generated events were scaled wrt the MC True generated events for the 75 cm cut passing rates due to only running over 188,880 generated events versus the 191362 generated events. The last column Signal:Cosmic only gives an estimate of the ν_μ CC events wrt the cosmic only background at each step. For this number, the cosmic background has been scaled as described in [?]. Note that these numbers are not a purity, since other backgrounds can't be determined at this step.

Signal	ν_μ CC events with true vertex in FV	#Events(Fraction) passing CNN @ 70% Probability	#Events(Fraction) passing CNN @ 83% Probability
		10605(35%)	6142(61%)
Backgrounds	Cosmics Only Events	13573(45%)	2582(26%)
	Cosmics in BNB Events	2249(7.4%)	492(4.9%)
	NC Events	3412(11%)	778(7.7%)
	ν_e and $\bar{\nu}_e$ Events	139(0.5%)	32(0.3%)
	$\bar{\nu}_\mu$ Events	97(0.3%)	67(0.7%)

Table 10.2.: Signal and background event numbers at modified selection level with CNN cut estimated from a BNB+Cosmic sample and Cosmic only sample normalized to $5 * 10^{19}$ PoT. The last column gives the fraction of this signal or background type to the total selected events per CNN probability.

Table 10.1 shows the passing rates for the 75 cm track length cut and the CNN cut at 70% and 83%. The passing rates at the track containment level for the 75 cm track length cut compared to the CNN are comparable with only a 0.6% difference in the in time cosmic bin which may be due in part to the larger in time cosmic statistics used for the CNN dataset. These passing rates need to be comparable to then be able to compare the passing rates after the CNN cut to the 75 cm cut. Again, the same BNB+Cosmic sample was used for both selection I modified with 75 cm cut and

selection I modified with CNN cut. As it stands, a CNN cut at 83% probability has a MC true CC event passing rate of 14% compared to the 13% passing rate of the 75 cm track length cut. The Signal:Cosmic Only background is also reduced from 1:0.6 to 1:0.4. The total passing rate is also higher than the 75 cm cut, 3.6% vs 4.0%. Table 10.2 shows the breakdown of signal and backgrounds for the CNN at the different probabilities. We have a 61% signal passing rate with the CNN cut @ 83% versus the 53.8% signal passing rate of the 75 cm cut.

Based on these numbers, the following performance values of the modified selection with 75 cm cut versus modified selection with CNN @ 83% probability cut were calculated:

- Efficiency: Number of selected true ν_μ CC events divided by the number of expected true ν_μ CC events with interaction in the FV.
 - Selection I modified: 13%
 - Selection I modified with CNN cut @ 83% probability: 14%
- Purity: Number of selected true ν_μ CC events divided by sum of itself and the number of all backgrounds.
 - Selection I modified: 53.8%
 - Selection I modified with CNN cut @ 83% probability: 61%

Lastly, figure 10.14 shows a more representative performance of the CNN. Due to the fact that the CNN was trained on muons and pions, showing the performance of CC muon events versus NC pion events with respect to CNN probability gives a better picture of how the network is performing. Figure 10.14 shows that at 83% we are below the 75 cm cut NC pion threshold and still above the CC muon threshold. Using 83% probability not only reduced the NC pion background, it also dramatically reduced the in time cosmics and cosmics in the BNB.

10.5. Conclusions and Future Work

It was shown that even though CNN10000 was trained with single particle generated muons and pions, it performs fairly well at classifying track candidate images from BNB+Cosmic events. Events have been regained below the 75 cm track length cut and

Table 8: **Selection I: Modified** Signal and background event numbers at modified selection level estimated from a BNB+Cosmic sample and Cosmic only sample normalized to 5×10^{19} PoT. The last column gives the fraction of this signal or background type to the total 2189 selected events.

Signal	ν_μ CC events with true vertex in FV	#Events	
		1168	53.8%
Backgrounds	Cosmics only events	725	33.4%
	Cosmics in BNB events	144	6.6%
	NC events	75	3.5%
	ν_e and $\bar{\nu}_e$ events	4	0.2%
	$\bar{\nu}_\mu$ events	15	0.7%
	ν_μ CC events with true vertex outside FV	40	1.8%

Figure 10.13.: Snapshot of signal and background event numbers of Selection I modified from cc-inclusive note [?]

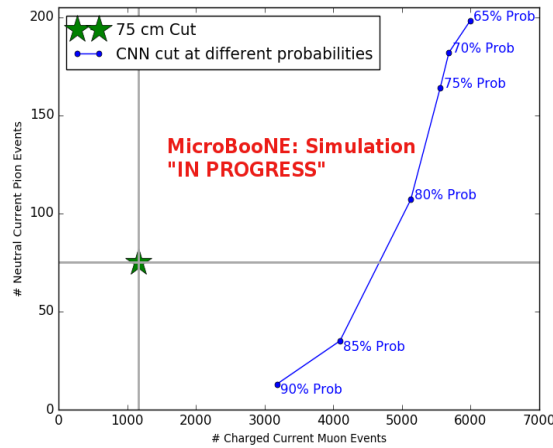


Figure 10.14.: CNN performance of classified muons and pions compared to the already implemented 75 cm track length cut

the momentum and track range distributions have similar shapes to the distributions of Selection I original and modified. Efficiencies and purities were calculated for selection I modified events before 75 cm track length cut with the CNN at 83% probability and are 14% and 62% respectively. Although the CNN doesn't have separation between muons and pions and although all particles passing CNN are classified as muon, increasing CNN probability allows us to increase the purity as well as maintain an efficiency comparable to the 75 cm track length cut all while recovering events below that 75 cm cut. Out of the 6142 events that passed the CNN @ 83% 1470 events were below the 75 cm cut, a recovery of 3.3% of data with an purity of 15%. Although these numbers are low, it is an improvement from the selection I modified in both total efficiency and purity and an increase in phase space by recovering these events. The next steps are to train two additional neural networks. One with track candidate muon and pion images originating from BNB+Cosmic events and the second whole CC_μ/NC_π events to gauge CNN performance. These trainings are underway.

Chapter 11.

Using Convolutional Neural Networks on MicroBooNE Data

...

...

Chapter 12.

Comparing two CC-Inclusive Cross Section Selection Filters

...

...

Chapter 13.

Conclusion

Your Conclusions here.

Appendix A.

Pointless extras

*“Le savant n’étudie pas la nature parce que cela est utile;
il l’étudie parce qu’il y prend plaisir,
et il y prend plaisir parce qu’elle est belle.”*
— Henri Poincaré, 1854–1912

Appendixes (or should that be “appendices”?) make you look really clever, ’cos it’s like you had more clever stuff to say than could be fitted into the main bit of your thesis. Yeah. So everyone should have at least three of them. . .

A.1. Like, duh

Padding? What do you mean?

A.2. $y = \alpha x^2$

See, maths in titles automatically goes bold where it should (and check the table of contents: it *isn’t* bold there!) Check the source: nothing needs to be specified to make this work. Thanks to Donald Arsenau for the teeny hack that makes this work.

Bibliography

- [1] Wikipedia, Neutrino, <http://wikipedia.org/wiki/Neutrino>, 2013.
- [2] Wikipedia, Neutrino oscillation, http://en.wikipedia.org/wiki/Neutrino_oscillation, 2013.
- [3] B. N. Laboratory, Neutrinos and nuclear chemistry, <http://www.chemistry.bnl.gov/sciandtech/sn/default.htm>, 2010.
- [4] K. Heeger, Big world of small neutrinos, <http://conferences.fnal.gov/lp2003/forthepublic/neutrinos/>.
- [5] A. Y. Smirnov, p. 23 (2003), hep-ph/0305106.
- [6] The MicroBooNE Collaboration, R. e. a. Acciari, (2015), arXiv:1512.06148.
- [7] The MicroBooNE Collaboration, R. e. a. Acciari, (2016), arXiv:1705.07341.
- [8] The MicroBooNE Collaboration, R. e. a. Acciari, (2017), arXiv:1704.02927.
- [9] The MicroBooNE Collaboration, R. e. a. Acciari, JINST 12 (2017).